Earth and Space Science

RESEARCH ARTICLE

Key Points:
- Surface downward longwave radiation (SDLR) was estimated based on the GBRT method
- SDLR increased at a rate of 1.3 Wm^2 per decade over China from 1958 to 2015
- SDLR trend is positively correlated with trends in T_a and water vapor pressure

Correspondence to:
X. Zhang,
xtngzhang@bnu.edu.cn

Trends and Variability of Atmospheric Downward Longwave Radiation Over China From 1958 to 2015

Yu Wei[1,2] , Xiaotong Zhang[1,2] , Wenhong Li[3] , Ning Hou[1,2], Weiyu Zhang[1,2], Jiawen Xu[1,2], Chunjie Feng[1,2], Kun Jia[1,2] , Yunjun Yao[1,2] , Jie Cheng[1,2] , Bo Jiang[1,2] , Kaicun Wang[4] , and Shunlin Liang[5]

[1]State Key Laboratory of Remote Sensing Science, Jointly Sponsored by Beijing Normal University and Institute of Remote Sensing and Digital Earth of Chinese Academy of Sciences, Beijing, China, [2]Beijing Engineering Research Center for Global Land Remote Sensing Products, Institute of Remote Sensing Science and Engineering, Faculty of Geographical Science, Beijing Normal University, Beijing, China, [3]Nicholas School of the Environment, Duke University, Durham, NC, USA, [4]Institute of Global Change and Earth System Science, Beijing Normal University, Beijing, China, [5]Department of Geographical Sciences, University of Maryland, College Park, MD, USA

Abstract Surface downward longwave radiation (*SDLR*) is a major component of the energy budget. Although studies have reported the spatiotemporal variations of *SDLR* in China, the spatiotemporal coverage of the situ measurements used is always limited. In this study, the gradient boosting regression tree (GBRT) was developed to reconstruct *SDLR* based on air temperature (T_a), relative humidity (RH), and downward shortwave radiation (*DSR*). Ground measurements collected at the Baseline Surface Radiation Network (BSRN) and the Arid and Semi-arid Region Collaborative Observation Project (ASRCOP) were used to build and evaluate the GBRT model. The evaluation results showed that the daily *SDLR* estimates are correlated well with the *SDLR* in situ, with an overall root mean square errors (RMSE) of 16.5 Wm^{-2} and a correlation coefficient (*R*) value of 0.91 for the validation data set. Comparison with existing *SDLR* products showed that accuracy and trends of the *SDLR* estimates based on the GBRT method are reasonable. To obtain long-term *SDLR* data for spatiotemporal analysis over China, densely distributed reconstructed *DSR* and ground measured T_a and RH collected at 756 Chinese Meteorological Administration (CMA) stations were used as input to estimate the *SDLR* based on the GBRT method over China during 1958–2015. The long-term estimated *SDLR*s at the selected 563 stations showed that *SDLR* increased at an average rate of 1.3 Wm^{-2} per decade over China from 1958 to 2015. The trend of *SDLR* is positively correlated with the trend in T_a and water vapor pressure, whereas negatively correlated with the trend in *DSR*.

1. Introduction

Surface downward longwave radiation (*SDLR*) is a fundamental component of the Earth's radiation budget (Iziomon et al., 2003). Understanding of *SDLR* variation is vitally important for weather prediction, energy budget evaluations, and numerous applications, such as predicting evapotranspiration and temperature variations (Flerchinger et al., 2009). *SDLR* is mainly emitted by H_2O, CO_2, and O_3 molecules and cloud water droplets in the atmosphere (Guo et al., 2019). *SDLR* is considered to be an important forcing on the Earth's surface energy budget that can produce surface warming (Burt et al., 2016; Woods & Caballero, 2016; Zeppetello et al., 2019). Additionally, it is essential for understanding the impact of increasing CO_2 and other greenhouse gases on the climate (Stephens et al., 1994).

SDLR is not conventionally measured, because it is difficult and expensive to measure directly (Duarte et al., 2006; Enz et al., 1975; Sridhar & Elliott, 2002; K. C. Wang & Liang 2009a). Consequently, different parameterization schemes have to be developed that take more readily available meteorological values as input. The weighting function of *SDLR* peaks near the surface, and correctly calculating the air temperature close to the surface is critical for *SDLR* estimation (Gupta et al., 2004). Previous studies showed that under clear sky conditions, the distributions of air temperature (T_a) and humidity are most important for *SDLR* estimation (Cheng et al., 2017). T_a and surface water vapor pressure measured close to the ground are used for *SDLR* estimation in the parameterization schemes under clear sky conditions (Brunt, 1932; Brutsaert, 1975; Idso, 1981; Swinbank, 1963). However, the coefficients for the parameterization schemes are often specific

for a limited range of climate regions and atmosphere conditions under which they were calibrated and validated. The parameterization scheme should be redefined or calibrated before it is used in other places (Bilbao & De Miguel, 2007). Retrievals of T_a and relative humidity (RH) profiles from satellite observations are also employed to estimate *SDLR* (Ellingson, 1995). Radiative transfer models (e.g. LOWTRAN or MOD-TRAN), named physical based methods, have been used to describe the actual emission and absorption processes in the atmosphere and to estimate *SDLR* (Duarte et al., 2006). Darnell et al. (1983) estimated *SDLR* based on Television and Infrared Observation Satellite (TIROS) Operational Vertical Sounder (TOVS) data obtained from the National Oceanic and Atmospheric Administration (NOAA). Although these physical based methods have explicit physical basis, the accuracy of the input parameters may directly affect the estimation accuracy. It is also very difficult to obtain temperature and humidity profiles of the lower atmosphere at stations with the accuracy required for *SDLR* estimation (Duarte et al., 2006; Ellingson, 1995; K. Wang & Dickinson 2013; K. C. Wang & Liang 2009a). Moreover, the physical based methods may not be suitable for cloudy sky conditions since clouds are always impenetrable in the thermal infrared spectrum as pointed by K. C. Wang and Liang (2009a). For example, most passive satellite sensors can only provide observations of the cloud top, but *SDLR* is more closely related to the parameters of cloud base (Ellingson, 1995).

Most existing parameterization schemes use cloud cover fraction to quantify the contribution of clouds to *SDLR*, which is proportional to the total cloudiness (Aladosarboledas, 1993; Bilbao & De Miguel, 2007; Ellingson, 1995; Niemela et al., 2001). Meteorological observations and satellite cloud detection products can provide reliable cloud cover fraction measurements (Ackerman et al., 2008). For example, Diak et al. (2000) proposed a parameterization for *SDLR* estimation under cloudy sky conditions, in which the cloud product collected from the Geostationary Operational Environment Satellite (GOES) was used to quantify the influence of clouds. This parameterization method showed an overall root mean square error (RMSE) value of 20 Wm^{-2} against the ground measurements. The cloud cover fraction can alternatively be represented by the ratio of the measured horizontal global solar radiation to the horizontal global solar radiance under clear sky conditions (Crawford & Duchon, 1999). Downward shortwave radiation (*DSR*) can reflect the contribution of cloud to the *SDLR*. Crawford and Duchon (1999) proposed an improved parameterization scheme for calculating *SDLR* based on *DSR* measurements. K. Yang et al. (2010) estimated the *SDLR* based on calculating the cloud cover fraction using *DSR* estimated from a hybrid model. The evaluation analysis showed that the error of four Chinese Meteorological Administration (CMA) stations in the Tibetan Plateau (TP) was less than 30 Wm^{-2}. Most of the parameterization schemes under cloudy sky conditions strongly depend on the calibration data and do not fully consider the impact of cloud characteristics, such as the cloud base. Thus, it may also have larger biases outside the parameter range of their local calibration (K. Wang & Dickinson, 2013).

Besides these physical based methods, machine learning methods are alternative ways to estimate surface radiation (X. Y. Wang et al., 2017; Wei et al., 2019; L. Yang et al., 2018). Machine learning methods provide techniques that can automatically construct the relationship between input parameters and surface radiation by processing the available data and maximizing a problem dependent performance criterion. Wei et al. (2019) estimated the *DSR* using four machine learning methods based on Advanced Very High Resolution Radiometer (AVHRR) data. The evaluation results with ground measurements exhibited that the gradient boosting regression tree (GBRT) method was the most accurate. Unlike other machine learning methods, the GBRT method can automatically find nonlinear interaction via decision tree learning and achieve more accurate predictions (Johnson & Zhang, 2014). However, few studies have directly applied the GBRT method to estimate *SDLR* based on ground measurements, especially over China.

Many studies have been reported for estimating *SDLR* over China, including the parameterization methods (Yu et al., ; Yu et al., 2018), hybrid methods (B. Tang & Li, 2008; J. Wang et al., 2014; W. H. Wang & Liang, 2009b) and artificial neural networks (ANN) based methods (T. X. Wang et al., 2012; T. X. Wang et al., 2018). For example, Yu et al. () compared twelve and eight parameterizations methods under clear and cloudy sky conditions over Heihe River Basin in China, respectively. It showed that the estimated *SDLRs* based on the proposed schemes by Idso (1981) and Dilley and O'Brien (1998), and Maykut and Church (1973) performed best for the clear and cloudy sky conditions, respectively. J. Wang et al. (2014) developed an improved hybrid method to estimate *SDLR* over the TP using the Moderate-resolution Imaging Spectroradiometer (MODIS) observations under clear sky conditions. The estimated *SDLRs* based on the

proposed hybrid method have an overall RMSE value of 25.9 and 25.7 Wm^{-2} for the MODIS observations from Terra and Aqua, respectively. The ANN-based model was used to estimate *SDLR* over the TP by T. X. Wang et al. (2012). The model is comparable with or even better than existing algorithms, with an overall RMSE value of 20.1 Wm^{-2} and a bias value of −8.8 Wm^{-2}. Although much effort has been conducted on the improvements of the methods for *SDLR* estimation, studies on reconstructing the long-term *SDLR* datasets over China is still rare. Chang and Zhang (2019) reconstructed *SDLR* data sets at 351 stations over China. He et al. (2020) developed the China Meteorological Forcing Data set (CMFD) based on the ground measurements at 753 CMA stations from 1979 to the present. The *SDLR* forcing data set was estimated based on the semi-empirical method proposed by Crawford and Duchon (1999), which calculated the atmospheric emissivity as a function of cloud amount and T$_a$. The temporal coverage of the estimated *SDLR* by the released methods is limited and the spatiotemporal analysis of *SDLR* over China is not well discussed. To improve our understanding of the climate change, it is still necessary to reconstruct a comprehensively spatiotemporal extended *SDLR* data set over China and computed spatiotemporal analysis based on this data set.

The physical relationship between the T$_a$, RH, *DSR,* and *SDLR* is fairly well known. In particular, Cheng et al. (2017) and Zeppetello et al. (2019) have shown that near surface air temperature is the prominent driver of both clear and all-sky downward longwave radiation in observations and climate models respectively. The radiative kernels presented by Previdi (2010) and Pendergrass et al. (2018) also present clear physical explanations for the relationship between *SDLR* and meteorological variables, including T$_a$ and RH. *SDLR* estimation under cloudy sky conditions depends strongly on cloud condition. *DSR* can be used to quantify the contribution of clouds to *SDLR* under cloudy sky conditions (Crawford & Duchon, 1999; K. Yang et al., 2010). Crawford and Duchon (1999) calculated cloud fraction from *DSR* under clear and cloudy conditions. Thus, T$_a$, RH, and *DSR* measurements are selected as input variables of the GBRT method in this study.

There are a total of 756 CMA meteorological stations where T$_a$, RH, and other surface meteorological parameters are measured, and all these data are available to the public. Compared with 756 routine meteorological stations, only 122 have global solar radiation measurements. Among 122 radiation observation stations, only 48 have relatively complete record from 1970 to 2015 through statistics. It is clear that the current existing radiation observation stations have relatively low spatial coverage and representativeness for long-term analysis. Therefore, the objectives of this study are: (1) to estimate *SDLR* using ground measurements. Ground measurements collected at the Baseline Surface Radiation Network (BSRN) and the Arid and Semi-arid Region Collaborative Observation Project (ASRCOP) were used to build and evaluate the GBRT model, respectively; and (2) to analyze the spatial pattern and temporal variations of the *SDLR* over China. To obtain long-term and densely distributed *SDLR* data over China for subsequent spatiotemporal analysis, the reconstructed long-term *DSR* (Hou et al., 2020), and the ground measured T$_a$ and RH collected at 756 CMA stations from 1958 to 2015 were used as input of the proposed GBRT method. The accuracy and trend evaluation results of the *SDLR* estimates based on the GBRT method are also compared with existing *SDLR* products.

This paper is organized as follows: In Section 2, the ground measurement data used in this paper are described. The machine learning method and trend test method are described in Section 3. The results are presented in Section 4. In Section 5, we discuss the correlation between the trends of estimated *SDLRs* and other variables (such as T$_a$). The conclusions are given in Section 6.

2. Data

2.1. Ground Measurements

The data records at BSRN stations have been reported to show a higher level of data quality (Liang et al., 2010). The ground measurements collected at the BSRN were used to build the model, including daily *DSR* (Wm^{-2}), *SDLR* (Wm^{-2}), air temperature (T$_a$, °C) at 2 m height, relative humidity at 2 m height (RH, %), and elevation (m). Since the *SDLR* ground measurements are not provided at the CMA stations, the ground measured *SDLR* collected at the ASRCOP stations was used to validate the robustness and accuracy
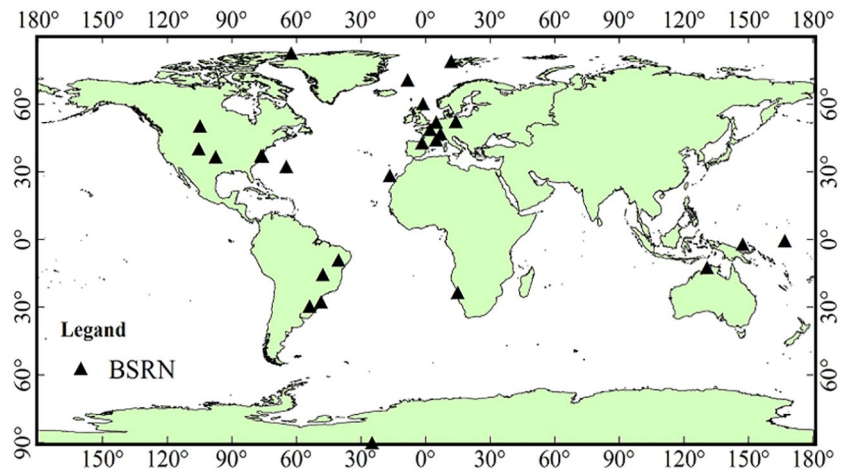
Figure 1. Spatial distribution of the radiation stations provided by the BSRN. BSRN, Baseline Surface Radiation Network.

of the model. Ground measurements collected at the CMA from 1958 to 2015 were used to derive the *SDLR* estimates over China in this study.

1. *BSRN*: The BSRN was initiated by the World Climate Research Programme (WCRP) to provide validation material for satellite radiometry and climate models. The BSRN operation started in 1992 at nine stations and currently consists of more than 60 operational stations (Ohmura et al., 1998). Recent reports have indicated that the BSRN measurements have the highest possible accuracy and a high temporal resolution in various climate zones and with uncertainties of approximately $\pm 5 \, \mathrm{Wm}^{-2}$ (Liang et al., 2010). Data extracted at 25 stations, which provide both *DSR* and *SDLR* records from 2000 to 2015, were used to train the model in this study. The spatial distribution of the data is shown in Figure 1

2. *ASRCOP*: The ASRCOP provides pyranometer data from 18 China meteorological stations in the summers of 2008 and/or 2009. The observed *SDLR* and meteorological data at the ASRCOP stations were recorded with a temporal resolution of 10 or 30 min (Cheng & Liang, 2016; Huang et al., 2013). Data collected from nine stations were used to evaluate the accuracy of the estimation model. Figure 2 and Table 1 show the spatial distribution and detailed information of these stations

3. *CMA*: There are a total of 756 CMA meteorological stations where daily T_a, the RH and other surface meteorological parameters are measured, and all these data are available to the public. Among these stations, only 122 have global solar radiation measurements. Figure 2 shows the spatial distribution of these routine meteorological and radiation stations. Solar radiation measurements at the CMA stations started in 1957. Since 1994, only 96 stations continued to measure solar radiation as the measurements at various stations stopped over the years (W. J. Tang et al., 2013). It is noted that there were two different types of radiometers equipped at the CMA stations before 1994 and afterward. Solar radiation measurements are more prone to errors and often encounter more problems, such as technical failures and operation-related problems, than other meteorological variable measurements (Moradi, 2009; W. J. Tang et al. 2010). Therefore, data quality control is indispensable for many applications. In this study, the quality control procedure proposed by Zhang et al. (2015) was performed

2.2. Existing *SDLR* Products

Existing *SDLR* products are used for comparison with the *SDLR* estimates based on the GBRT method. Considering the time series and accuracy of different *SDLR* products, CERES-SYN *SDLR* product were used to compare accuracy on ASRCOP stations, the ERA5 and GEWEX-SRB *SDLR* products were used for comparison of long-term trend. The brief introduction of three *SDLR* products are as follows:

1. *GEWEX-SRB*: The latest version of GEWEX-SRB (v3.0) is applied in this study. The GEWEX-SRB *SDLR* data can be available from July 1983 to December 2007 at a 3-hourly resolution, which are then averaged
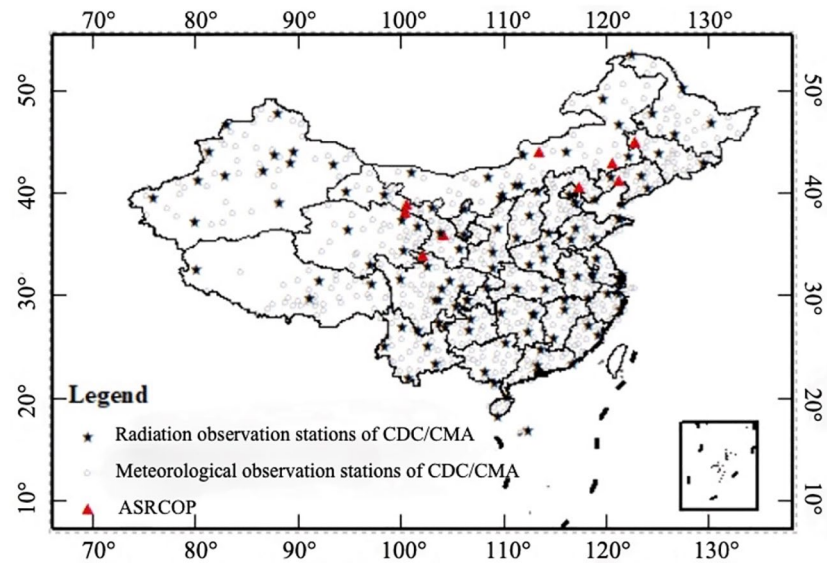
Figure 2. Spatial distribution of the radiation stations provided by the ASRCOP and CMA. ASRCOP, Arid and Semi-arid Region Collaborative Observation Project; CMA, Chinese Meteorological Administration.

into daily, monthly values. The data set is produced on a 1º × 1º global grid using satellite-derived cloud parameters and ozone fields, reanalysis meteorology, and a few other ancillary data sets (Cox et al., 2006). Based on their official Web site, the overall daily mean bias for GEWEX-SRB is 0.5 Wm^{-2} and the RMSE is 21.8 Wm^{-2} compared to BSRN measurements from 1992 through 2007. These values are −0.1 and 11.2 Wm^{-2} at the monthly time scale

2. *CERES-SYN*: CERES (Clouds and the Earth's Radiant Energy System) SYN (Synoptic Radiation Fluxes and Clouds) product sponsored by National Aeronautics and Space Administration (NASA) were designed to study the earth's top-of-atmosphere (TOA), on surface and within the atmosphere radiation budgets (Doelling et al., 2013; Ohmura et al., 1998). Data used in this study for comparison with the *SDLR* estimates based on the GBRT method are available from March 2000 to present with a spatial resolution of 1º × 1º and a daily temporal resolution

3. *ERA5*: ERA5 data on single levels are the fifth-generation ECMWF atmospheric reanalysis of the global climate, covering the period from 1979 to present (Hersbach & Dee, 2016; Naseef & Kumar, 2008). The data can be available on the time resolution of hourly and monthly with the spatial resolution of 0.25° × 0.25°. Reanalysis combines model data with observations from across the world into a globally complete and consistent data set using the laws of physics

Table 1
Basic Summary of the ASRCOP Stations Used to Validate the Model

Station	Latitude (°)	Longitude (°)	Elevation (m)	Land cover	Time period
Arou	38.04	100.46	3,033	Desert/grassland	2008–2009
Dongsu	44.09	113.57	970	Desert/grassland	2008–2009
Jinzhou	41.18	148.48	22	Farmland	2008–2009
Maqu	33.89	102.14	3,423	Wetlands	2008
Miyun	40.63	117.32	350	Farmland	2008–2009
Tongyu grass	44.58	122.92	184	Grassland	2008–2009
Tongyu farmland	44.59	122.93	184	Farmland	2008–2009
Yingke	38.86	100.41	1,519	Farmland/oasis	2008–2009
Yuzhong	35.95	104.13	1,965	Desert/grassland	2008–2009

2.3. Reconstructed *DSR* Data set over China

The reconstruction data set of long-term *DSR* over China from Hou et al. (2020) was used as input to obtain long-term and densely distributed *SDLR* data over China. This data set was generated based on the random forest (RF) algorithm using the ground measured *DSR* data and the routine meteorological station data collected at 756 CMA stations. This data set was available from 1958 to 2015 with a daily time resolution. The *DSR* estimates are validated using the ground measurements with a correlation coefficient (R) value of 0.99, a bias value of 0.01 Wm^{-2}, and an RMSE value of 8.88 Wm^{-2}. The reconstructed *DSR* data set is also reasonably accurate compared to the existing reconstructed data set.

3. Method

3.1. Gradient Boosting Regression Tree

The GBRT algorithm can be considered as an improved version of boosting that is based on iteratively constructing multiple individual decision trees. Boosting is an ensemble learning algorithm which combined a series of weak classifiers into a strong classifier according to different weights. The basic idea of GBRT algorithm is to establish a new regression model in the direction of gradient reduction, and to form a regression tree model through continuous iterations. The main advantage of the GBRT algorithm is that it can automatically find nonlinear interactions via decision tree learning, and it has relatively few tuning parameters as a nonlinear learning scheme (Johnson & Zhang, 2014).

Assuming that x_i is a set of predictor variables, y_i is a set of response variables, and N is the number of training samples. The GBRT method constructs M different individual decision trees $h(x;a_1)$, $h(x;a_2)$,..., $h(x;a_M)$, then $h(x;a_m)$ can be used as the basic function to express the approximation function $f(x)$ as follows (Ding et al. 2016):

$$\begin{cases} f(x) = \sum_{m=1}^{M} f_m(x) = \sum_{m=1}^{M} \beta_m h(x;a_m) \\ h(x;a_m) = \sum_{j=1}^{J} \gamma_{jm} I(x \in R_{jm}), where\ I = 1\ if\ x \in R_{jm}; I = 0, \text{otherwise} \end{cases}, \qquad (1)$$

where β_m and α_m represent the weight and classifier parameter of each decision tree, respectively. The loss function $L(y, f(x))$ is used to describe the accuracy of β_m and α_m. Each tree partitions the input space into J regions R_{1m}, R_{2m},..., R_{jm}, and each R_{jm} predicts the constant γ_{jm}. The main flowchart of the GBRT method is shown in Figure 3. In this study, the GBRT method is implemented using the scikit-learn toolbox on the Python platform (Pedregosa et al., 2012). The main flowchart of this study is shown in Figure 4.

3.2. Mann-Kendall (MK) Trend Test

The nonparametric MK statistical test (Kendall, 1938; Mann, 1945) has been employed to detect trends in different hydrological and meteorological time series. Compared to linear regression trend analysis, the MK trend test is more suitable for cases where the trend may be assumed as a monotonic and normal distribution (Zhou et al., 2018). The test statistic S is given by (Gocic & Trajkovic, 2013):

$$S = \sum_{i=1}^{n-1} \sum_{j=i+1}^{n} \text{sgn}(x_j - x_i), \qquad (2)$$

$$\text{sgn}(x_j - x_i) = \begin{cases} +1, if\ x_j - x_i > 0 \\ 0, if\ x_j - x_i = 0 \\ -1, if\ x_j - x_i < 0 \end{cases}, \qquad (3)$$

where n, x_i, x_j represent the number of data points, data values in the time series i and $j(j > i)$, respectively.

Initialize $\quad f_0(x) = \arg\min_\rho \sum_{i=1}^{N} L(y_i, \rho)$

For m = 1 to M do

    For i = 1 to n do

        Compute the negative gradient $\quad \tilde{y}_{im} = -\left[\dfrac{\partial L(y_i, f(x_i))}{\partial f(x_i)}\right]_{f(x)=f_{m-1}(x-1)}$

    End;

    Fit a regression tree $h(x; a_m)$ to predict the targets $\tilde{y}_{im}$ from covariates x_i for all training data

    Compute a gradient descent step size as $\quad \rho_m = \arg\min_\rho \sum_{i=1}^{n} L(y_i, f_{m-1}(x_i) + \rho h(x_i; a_m))$
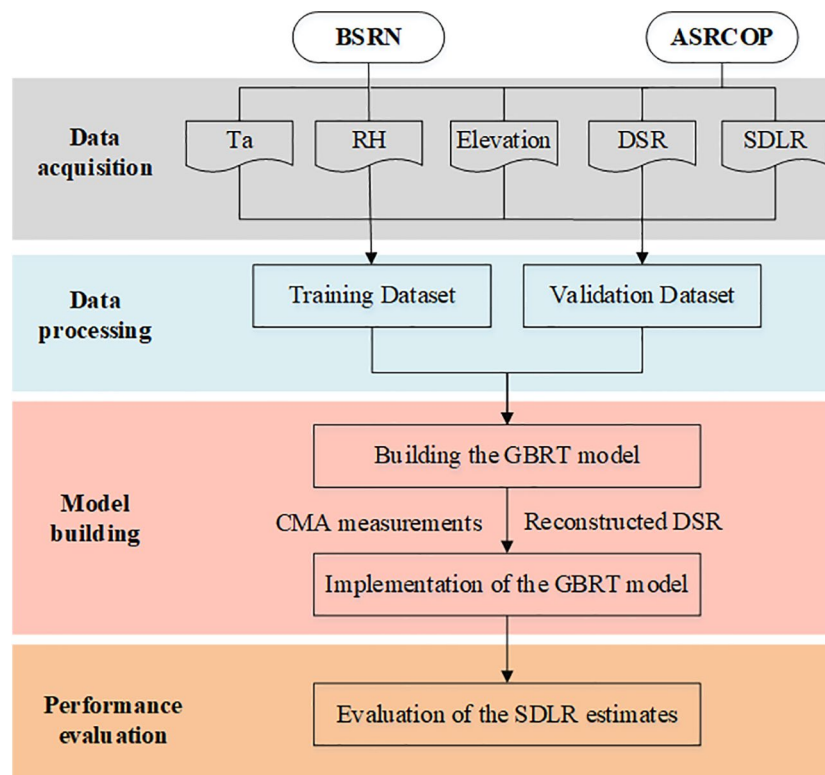
    Update the model as $\quad f_m(x) = f_{m-1}(x) + \rho_m h(x_i; a_m)$

End;

Output the final model $\quad f_M(x)$

Figure 3. The main flowchart of the GBRT method. GBRT, gradient boosting regression tree.

Figure 4. The main flowchart of this study.

Table 2
Parameters Setting to Determine the Optimal Parameters for the GBRT Method

Parameters	Threshold	Intervals
Learning rate	0.1–0.9	0.1
Subsample	0.2–1	1
Max depth	4–9	5
n-Estimators	50–350	250

The variance is computed as:

$$\text{Var}(S) = \frac{n(n-1)(2n+5) - \sum_{i=1}^{m} t_i(t_i-1)(2t_i+5)}{18}, \tag{4}$$

where n and m are the number of data points and tied groups, respectively, and t_i denotes the number of ties of extent i. A tied group is a set of sample data with the same value. In cases where the sample size is $n > 10$, the standard normal test statistic Z_S is expressed as (Zhou et al., 2018):

$$Zs = \begin{cases} \dfrac{S-1}{\sqrt{\text{Var}(S)}}, & if \quad S > 0 \\ 0, & if \quad S > 0, \\ \dfrac{S+1}{\sqrt{\text{Var}(S)}}, & if \quad S < 0 \end{cases} \tag{5}$$

In a two-tailed test, the null hypothesis of no trend should be accepted at a specific significance level for $-Z_{1-\alpha/2} \leq Zs \leq Z_{1-\alpha/2}$, where $Z_{1-\alpha/2}$ is the standard score of the standard normal distribution with a cumulative probability of $1 - \alpha / 2$. Otherwise, the null hypothesis of no trend is rejected, and a monotonic trend is identified at significance level α. Positive values of Z_S indicate increasing trends, while negative Z_S values indicate decreasing trends. In this study, $a = 0.05$ was taken to identify a significant trend which means that $Z_{1-\alpha/2} = \pm 1.96$.

In this study, we used the Sen's slope to describe the steepness of the trend in long time series, which is computed as (Sen, 1968):

$$Q_i = \frac{x_j - x_k}{j-k} \text{ for } i = 1,\ldots,N, \tag{6}$$

$$\text{Slope} = \begin{cases} Q_{\left[(N+1)/2\right]}, & if \ N \text{ is odd} \\ \dfrac{Q_{\left[(N)/2\right]} + Q_{\left[(N+1)/2\right]}}{2}, & if \ N \text{ is even} \end{cases}, \tag{7}$$

where N is the number of data pairs, x_j and x_k are the data values at times j and k ($j > k$), respectively. The N values of Q_i are ranked from smallest to largest.

3.3. Model Construction

The GBRT model can be constructed in three steps.

(1) *Preparation of the training datasets*: Four variables extracted at the BSRN stations were used as predictor variables, including elevation, daily T_a, daily RH, and daily *DSR*. The daily *SDLR* measurements were used as target variables

(2) *Configuration of the model coefficients*: We used the k-fold cross validation method to determine the optimal parameters. Each parameter is traversed in range of parameter threshold, as shown in Table 2. The error of predicted results is evaluated against ground measurements and parameters providing the highest average R in the training data set were selected as optimal parameters. The GBRT model is influenced by the number of iterations, learning rate, depth of the tree, and sampling rate. The learning rate parameter limits the contribution of each tree. A small learning rate parameter can reduce overfitting. A larger iteration number parameter means more boosting stages to perform and usually provides better performance for the training data set. The iteration number parameter should be carefully set to avoid overfitting. Moreover, there is a trade-off between the learning rate and iteration number. The model complexity and computational cost increase with increasing iteration number and decreasing learning rate, leading to a poor prediction performance. The tree depth represents the maximum depth of the individual regression estimators which can limit the number of nodes in the tree. The sampling rate parameter represents the fraction of training samples used for fitting. A subsample parameter smaller than 1.0 can prevent overfitting and reduce the variance. Successive performance testing showed that a
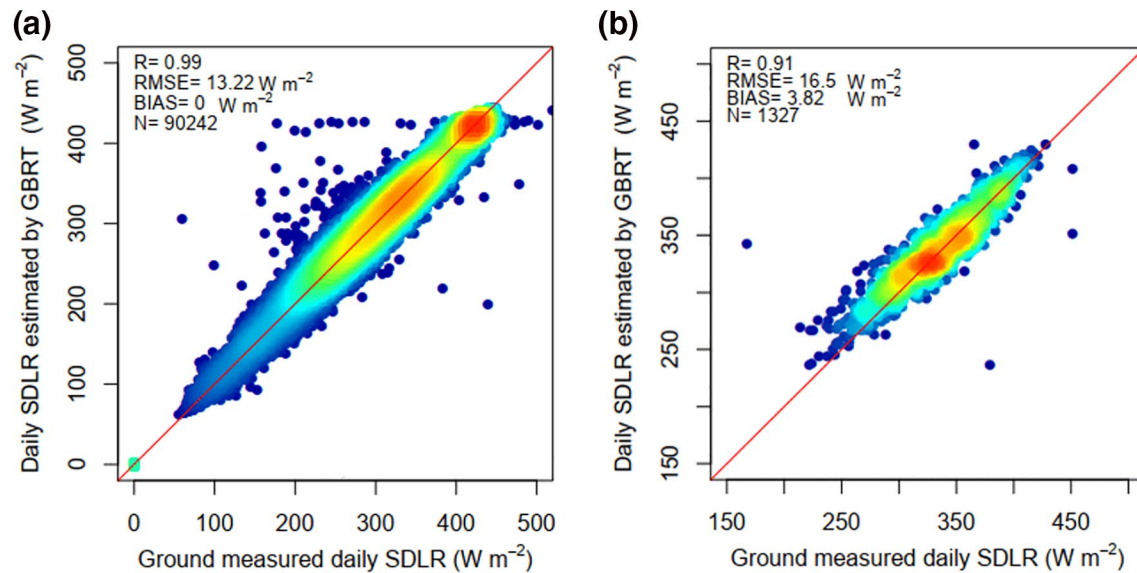
Figure 5. Evaluation results of the (a) BSRN training and (b) ASRCOP validation data set's daily *SDLR* estimates based on the GBRT method against ground measurements. *N* is the number of total data points. ASRCOP, Arid and Semi-arid Region Collaborative Observation Project; BSRN, Baseline Surface Radiation Network; GBRT, gradient boosting regression tree; SDLR, Surface downward longwave radiation.

GBRT model with a learning rate parameter of 0.1, a sampling rate of 1, a tree depth of 5, and an iteration number of 250 was optimal to estimate the *SDLR*

(3) *Application of the GBRT method*: After determining the optimal parameters, the performance of the trained model for the *SDLR* estimation was evaluated using ground measurements collected from the ASRCOP stations

4. Results and Analysis

4.1. Validation Against Ground Measurements

4.1.1. Validation of the *SDLR* Estimates

Ground measurements collected at 25 BSRN stations were used as the training data set to determine the optimal parameters. Then, daily *SDLR* measurements collected at nine ASRCOP stations in the summers of 2008 and/or 2009 were used as the validation data set to evaluate the performance of the GBRT method for the *SDLR* estimation. The selected BSRN stations are mainly concentrated in South America, North America, and Europe. Using ASRCOP data in China as the validation data set can validate the accuracy of the GBRT method without local correction, that is, validate the robustness of the model. Three statistical measures were used to evaluate the estimates against ground measurements, including overall RMSE, R, and bias.

The performance of the GBRT method for the estimation of daily *SDLR* are evaluated on BSRN training data set and ASRCOP validation data set, respectively. The evaluation results are shown in Figure 5. The daily *SDLR* estimates for the BSRN training data set have an overall RMSE value of 13.22 Wm^{-2}, a bias value of 0 Wm^{-2}, and an *R* value of 0.99, whereas these values are 16.5, 3.82 and 0.91 Wm^{-2} for the ASRCOP validation data set, respectively. The validation results for each ASRCOP station was further investigated to study the stability of the GBRT method, as shown in Figure 6. The daily *SDLR* estimates correlate well with the ground measurements at most ASRCOP stations, with the R values ranging from 0.76 to 0.96, the bias values ranging from −9.56 to 22.78 Wm^{-2}, and overall RMSE values ranging from 10.06 to 26.11 Wm^{-2}. Note that the *R* value is greater than 0.85 at eight out of nine stations and the absolute value of the bias is less than 10 Wm^{-2} at seven out of nine stations. The estimated *SDLRs* at Dongsu correlate best with the ground measurements, with an overall RMSE value of 10.06 Wm^{-2}, a bias value of −0.14 Wm^{-2}, and an *R* value of 0.96. These evaluation results further indicate that the *SDLR* estimates derived from the GBRT method correlate well with the ground measured *SDLRs*.
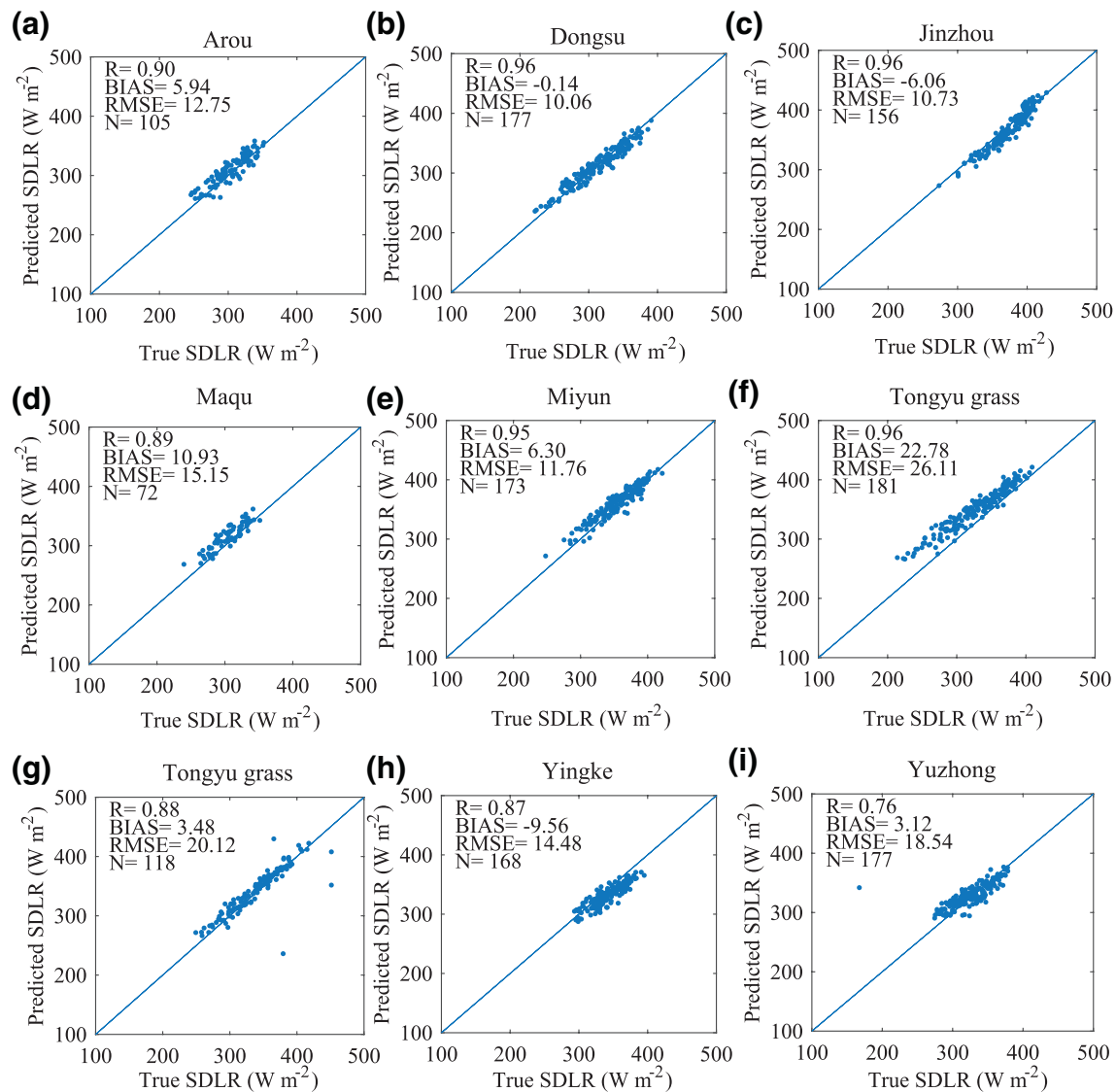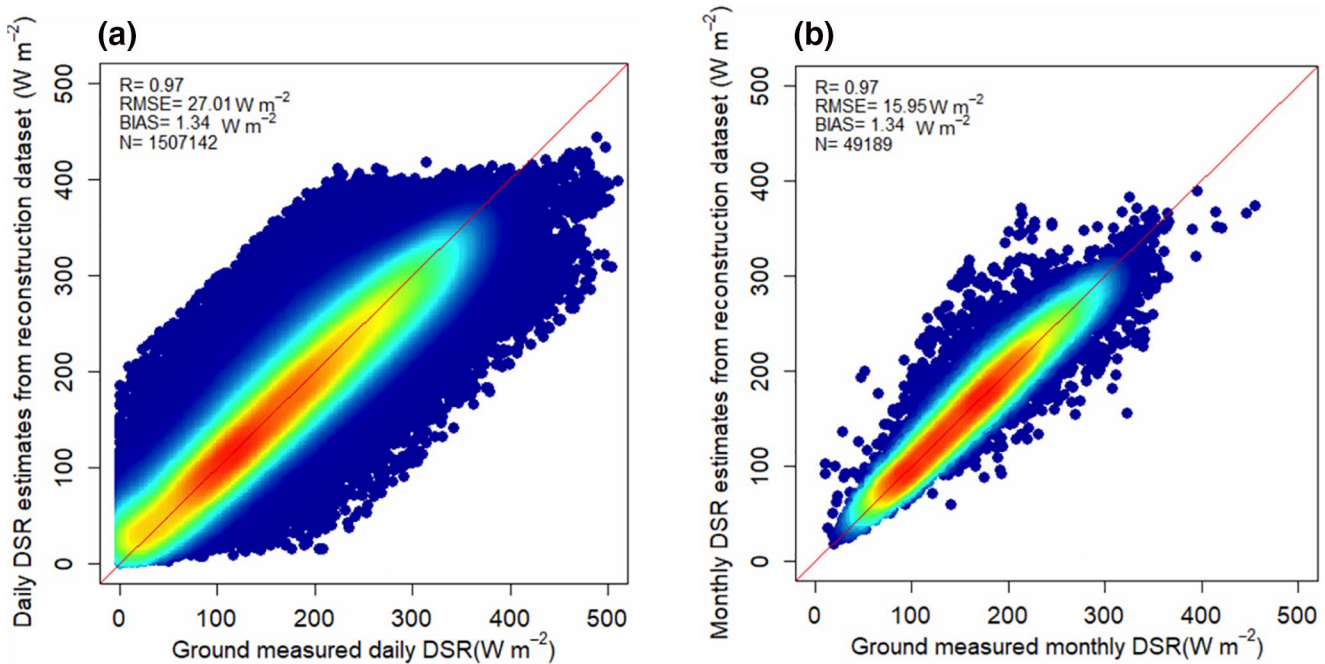
Figure 6. Evaluation results of daily *SDLR* estimates on each ASRCOP station based on the GBRT method against ground measurements. ASRCOP, Arid and Semi-arid Region Collaborative Observation Project; GBRT, gradient boosting regression tree; SDLR, Surface downward longwave radiation.

4.1.2. Validation of the Reconstructed DSR Dataset

In order to ensure the accuracy of the input variables of the machine learning method, the reconstructed long-term *DSR* data set over China from 1958 to 2015 was validated at the *DSR* ground measures collected at 122 CMA radiation stations. As shown in Figure 7, the *DSR* estimates from reconstructed data set have an *R* value of 0.95, a bias value of 1.34 Wm^{-2}, and an RMSE value of 27.01 Wm^{-2}, at a daily time scale. These values are 0.97, 15.95, and 1.34 Wm^{-2}, respectively, at a monthly time scale. Thus, the reconstructed *DSR* data set is reasonably accurate against the *DSR* ground measures.

### 4.2. Comparison with Existing *SDLR* Products

The CERES-SYN *SDLR* product was used to compare the evaluation results of *SDLR* estimates based on the GBRT method against ground measurements at ASRCOP stations in the summers of 2008 and/or 2009. As shown in Figure 8, the *SDLR* estimates based on the GBRT method correlate better with the ground measurements, with an overall RMSE value of 16.5 Wm^{-2}, a bias value of 3.82 Wm^{-2}, and an *R* value of 0.91.

Figure 7. Evaluation results of the reconstructed data set of long-term *DSR* over China based on the RF method at (a) daily and (b) monthly time scales. DSR, downward shortwave radiation; RF, random forest.

The CERES-SYN and ERA5 *SDLR* products all show lower accuracy. The CERES-SYN *SDLR* product has an overall RMSE value of 23.93 Wm^{-2}, a bias value of 7.95 Wm^{-2}, and an *R* value of 0.84. These values were 28.38, −7.29, and 0.74 Wm^{-2}, respectively, for the ERA5 *SDLR* product.

To further testify the *SDLR* estimates based on the GBRT method on 563 CMA stations, the RMSE and bias between daily SDLR estimates and ERA5 SDLR product are calculate at each CMA station from 1979 to 2015, as shown in Figures 9 and 10. The RMSE and bias range from 11.61 to 80.94 Wm^{-2} and −77.56 to 40.58 Wm^{-2}, respectively. There are 292 and 278 sites whose RMSE and bias values range from 20 to 25 Wm^{-2} and −10 to 0 Wm^{-2}, respectively; these are followed by 102 and 90 sites whose RMSE and bias values range from 25 to 30 Wm^{-2} and −20 to −10 Wm^{-2}, respectively. The lower RMSE values are mainly found in the Northeast and South China; while the higher RMSE values are mainly distributed in the Tibet Plateau and west of Southwest China, which may be due to the high altitude and harsh environment leading to large ground observation errors. There are 27 out of 563 sites whose biases are more than 30 Wm^{-2}, which may be due to the DSR estimates with relative big uncertainties at some stations. Moreover, the replacement of the CMA radiation instruments may also be a source of errors. It is worth to note that the spatial scaling issue would be another potential error sources for SLDR evaluation. We also compare the long-term trend of the *SDLR* estimates based on the GBRT method on 563 CMA stations with those from GEWEX-SRB and ERA5 products. The time period is set to 1984–2007 when all three *SDLR* datasets can be available. Figure 11 shows that the long-term trend of *SDLR* estimates based on the GBRT method (2.33 Wm^{-2} per decade, significant at 95% confidence) was similar to that from GEWEX-SRB (2.1 Wm^{-2} per decade, significant at 95% confidence), higher than that from ERA5 (1 Wm^{-2} per decade, significant at 95% confidence). Through the comparison of long-term trend with existing *SDLR* products, it is obvious that the *SDLR* estimates based on the GBRT showed a similar trend but different change magnitudes to existing *SDLR* products. Thus the temporal variations of *SDLR* based on the GBRT method on CMA stations are reasonable.
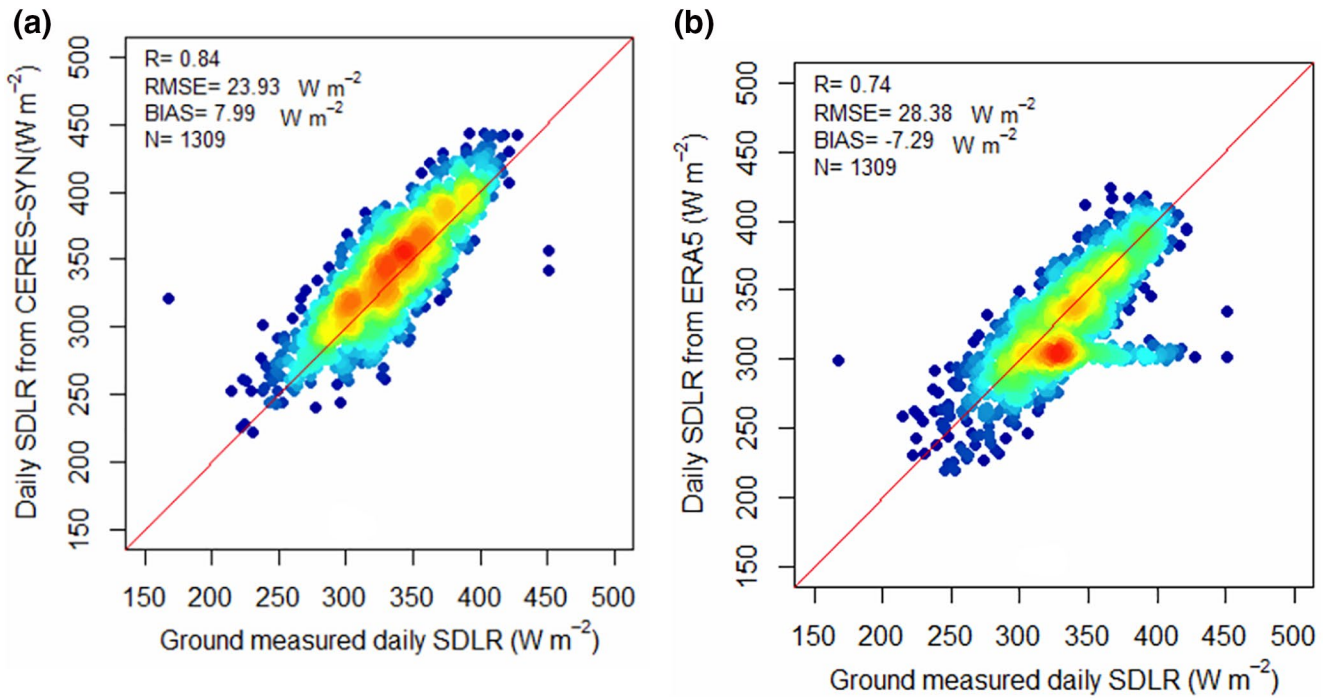
Figure 8. Evaluation results of daily *SDLR* estimates from (a) CERES-SYN and (b) ERA5 *SDLR* products on each ASRCOP station against ground measurements. ASRCOP, Arid and Semi-arid Region Collaborative Observation Project; CERES, Clouds and the Earth's Radiant Energy System; SDLR, Surface downward longwave radiation; SYN, Synoptic Radiation Fluxes and Clouds.

4.3. Spatial and Temporal Analysis of *SDLR* over China

The GBRT method used in this study performed well without a local correlation and only required surface meteorological and solar radiation data. Thus, we applied the GBRT method to obtain long-term and densely distributed *SDLR* data over China.
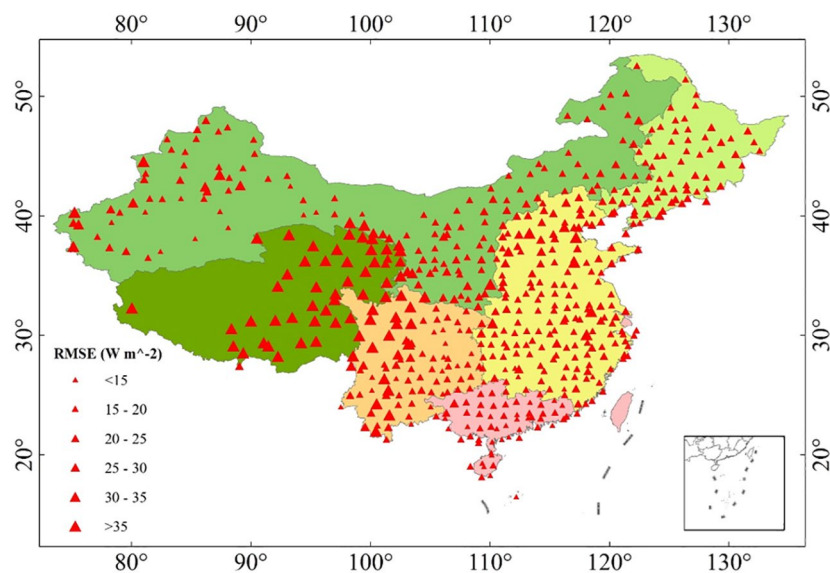

Figure 9. The RMSE between daily SDLR estimates and ERA5 SDLR products at 563 CMA stations from 1979 to 2015. CMA, Chinese Meteorological Administration; RMSE, root mean square errors; SDLR, Surface downward longwave radiation.
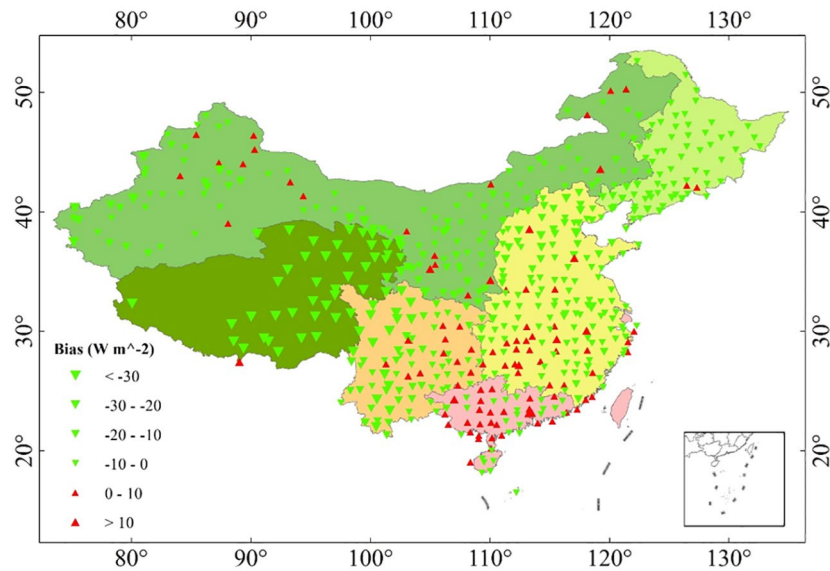
Figure 10. The Bias between daily SDLR estimates and ERA5 SDLR products at 563 CMA stations from 1979 to 2015. CMA, Chinese Meteorological Administration; SDLR, Surface downward longwave radiation.

Meteorological measurements and reconstructed *DSR* data set were used to estimate *SDLR* based on the proposed GBRT method. The input variables of the GBRT method were T_a, RH measurements, elevation of the stations, and reconstructed *DSR* values at 756 CMA stations from 1958 to 2015. Monthly *SDLR* estimates were obtained by averaging the daily values over the month. If there were more than 10 missing daily *SDLR* estimates in a month at a station, the data for this month at this station were deleted. Then, if there was less than one missing monthly *SDLR* estimate at one station in a year, the missing values were obtained by piecewise cubic Hermit interpolation to calculate annual values. Meanwhile, if there were less than two missing annual values for the time period at a station, the missing annual values at this station were also obtained by piecewise cubic Hermit interpolation. Otherwise, this station would be eliminated to study the long-term trends of *SDLR*. Therefore, 563 stations were used to analyze the spatial pattern and temporal variations of *SDLR* based on the completeness of the data records.
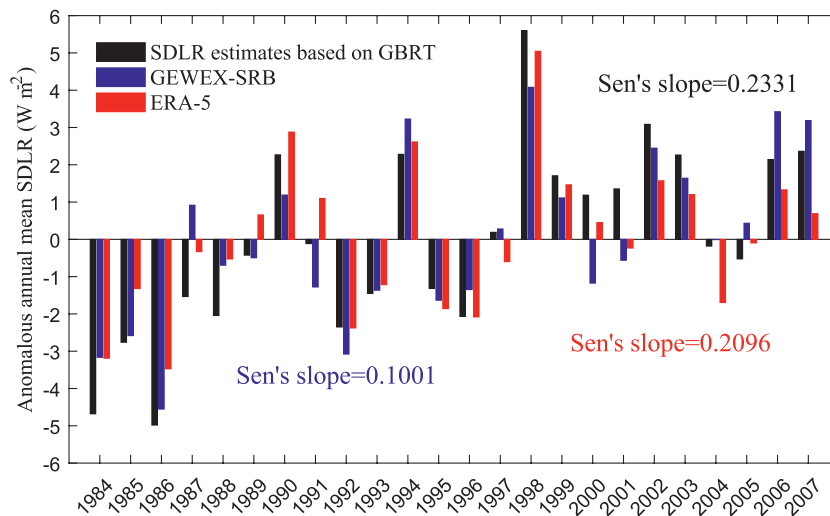
Figure 11. The comparison of anomalous annual mean *SDLR* estimates (unit: Wm^{-2}) averaged over mainland China from GBRT-based estimates, GEWEX-SRB and ERA5 *SDLR* products during 1984–2007. GBRT, gradient boosting regression tree; SDLR, Surface downward longwave radiation.
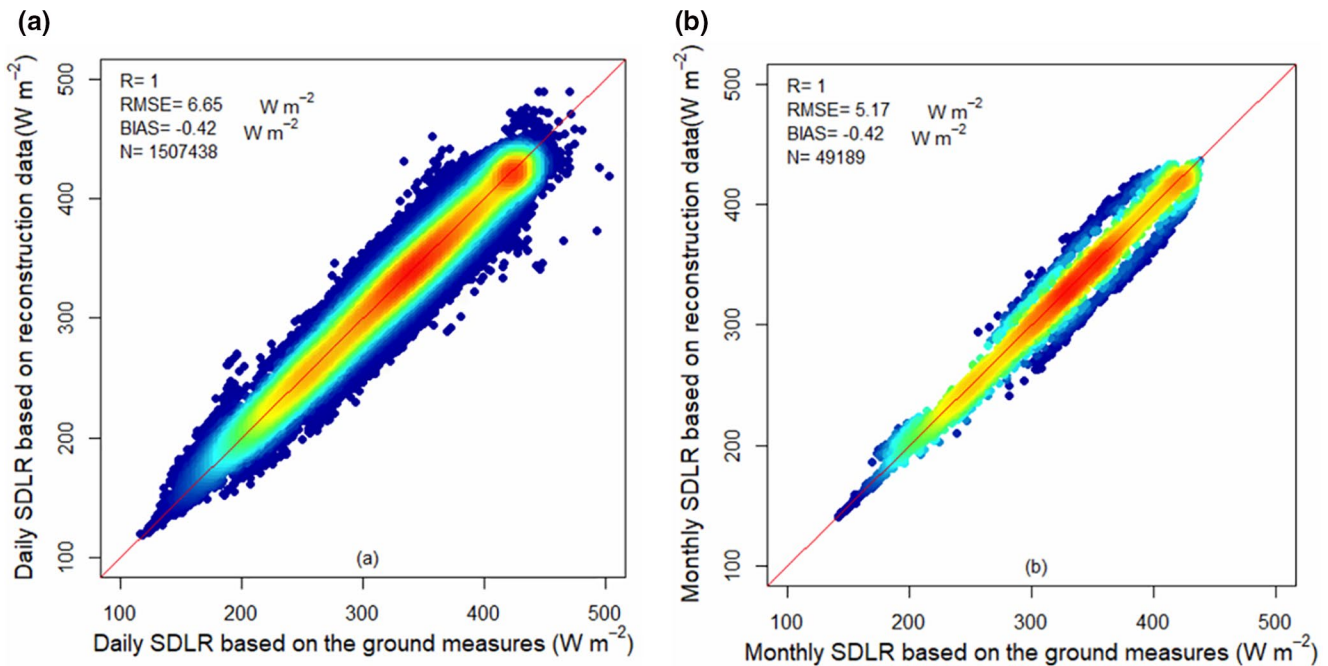
Figure 12. Evaluation results of the *SDLR* estimates based on the reconstructed *DSR* data set and which based on the *DSR* measure at (a) daily and (b) monthly time scales. DSR, downward shortwave radiation; SDLR, Surface downward longwave radiation.

4.3.1. Comparison with the SDLR Estimates Based on DSR Ground Measures

The *SDLR* estimates based on the reconstructed *DSR* data set was compared with which based on *DSR* ground measures at 122 CMA radiation stations from 1958 to 2015 to ensure the feasibility of spatiotemporal analysis. As shown in Figure 12, the *SDLR* estimates based on the reconstructed *DSR* data set correlate well with which based on the ground measures, with an *R* value of 1, a bias value of -0.42 Wm^{-2}, and an RMSE value of 6.65 Wm^{-2}, at a daily time scale. These values are 1, -0.42, and 5.17 Wm^{-2}, respectively, at a monthly time scale. Thus the error of the reconstructed data set has little effect on the accuracy of *SDLR* estimates based on the GBRT method. We also compare the long-term trend between the *SDLR* estimates based on the reconstructed and ground measured *DSRs*. Regarding the completeness of the *DSR* ground measures, the time series is determined to be 1970–2015 for comparison. 48 and 563 CMA stations were used for long-term trend analysis from 1970 to 2015 based on the reconstructed and ground measured *DSRs*, respectively. As shown in Figure 13, the *SDLR* estimates at CMA stations based on the reconstructed and ground measured *DSRs* show consistent trends from 1970 to 2015. The difference between anomalous annual mean *SDLR* estimates based on two *DSR* datasets was range from -0.02 to 3.09 Wm^{-2}, and the absolute values were within 1 Wm^{-2} in most years. The *SDLR* estimates used the *DSR* ground measurements as input showed significant increasing trends at a rate of 0.98 Wm^{-2} per decade from 1970 to 2015, while the value was 1.25 Wm^{-2} per decade for the *SDLR* estimates based on the reconstructed *DSR* data set. Thus, the *SDLR* estimates using reconstructed *DSR* data set as input can be used to perform spatiotemporal analysis of *SDLR* over China.

### 4.3.2. Spatial Distribution and Seasonal Variations of SDLR

According to the classification method of climatic types in China proposed by Zhou et al. (2018) and Liu et al. (2018), this study divided mainland China into six regions to compute spatiotemporal analysis, including East China (EC), North China (NC), Northeast China (NE), Southwest China (SW), South China (SC), and the TP. The spatial distribution and annual mean *SDLR* estimates of each region are presented in Figure 14. The different sizes and colors of the stations indicate the magnitude of the annual mean *SDLR* estimates at 563 CMA stations during 1958–2015. As it is shown in the figure, the annual mean *SDLR* estimates shows a pronounced latitudinal dependency except over the TP, with larger values at low latitudes and smaller values at high latitudes. This may be due to the low values of aerosol optical thickness and
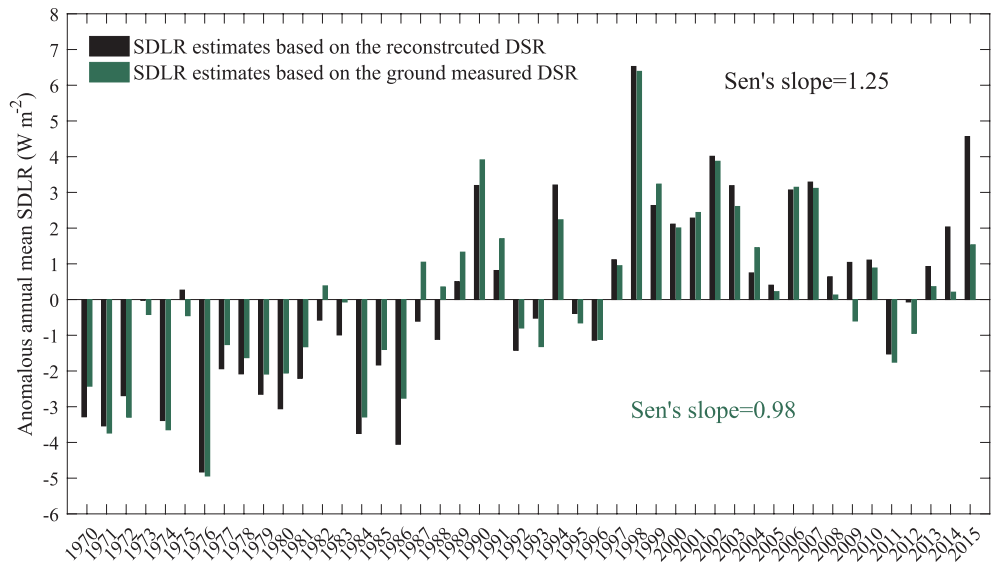
Figure 13. Comparison between the anomalous annual mean *SDLR* estimates (unit: Wm^{-2}) based on the *DSR* estimates and the *DSR* ground measures during 1970–2015. DSR, downward shortwave radiation; SDLR, Surface downward longwave radiation.

atmospheric water vapor content over the TP. Table 3 shows the annual mean *SDLR* estimates over China and six climate regions. EC, SC, and SW show higher annual mean *SDLR* than the other regions in China. The maximum annual mean *SDLR* estimates occur in SC, whereas the minimum value occurs in TP. The difference between the annual mean *SDLR* estimates in SC and TP is up to 100 Wm^{-2}.

Figures 15 and 16 show the monthly and seasonal mean *SDLR* estimates over mainland China and six subregions during 1958–2015, respectively. The monthly *SDLR* estimates gradually increase from January to July and then gradually decrease from July to December over both mainland China and six subregions. The highest seasonal mean *SDLR* typically occurs in summer, with areal averaged *SDLR* estimates of 379.20 Wm^{-2}. Following the same logic, the minimum *SDLR* occurs in winter, with values of 255.60 Wm^{-2}. The *SDLR* estimates show similar seasonal variation trends in all six subregions. The maximum seasonal
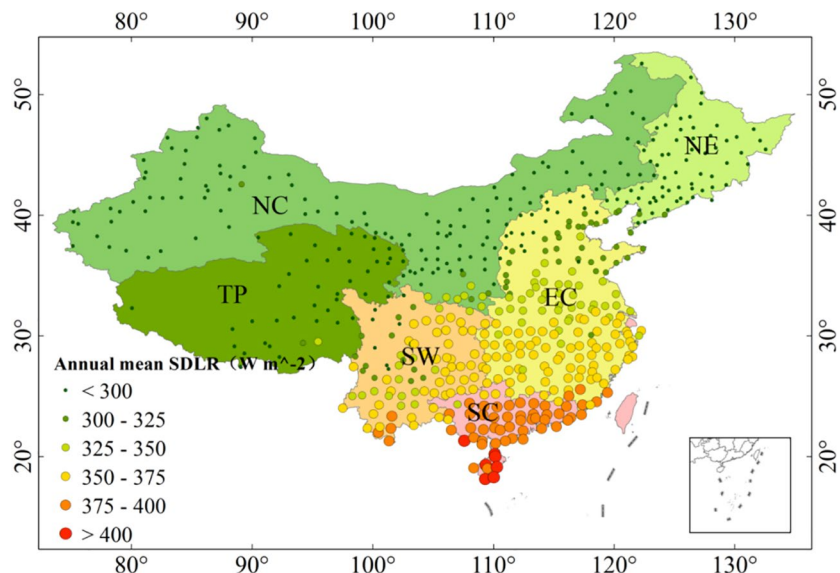
Figure 14. The annual mean *SDLR* estimates (unit: Wm^{-2}) at 563 CMA stations during 1958–2015. CMA, Chinese Meteorological Administration; SDLR, Surface downward longwave radiation.

Table 3
The Trends in Annual Mean SDLR Estimates Over Mainland China and Six Regions Detected by MK Test

Region	Annual mean *SDLR* (Wm^{-2})	1958–2015	1958–1990	1991–2015
China	316.14	1.02*	0.59	0.59
EC	336.74	1.07*	0.44	0.73
NC	277.06	1.30*	0.51	0.57
NE	278.31	1.31*	0.41	0.94
SC	384.22	0.61	0.53	0.10
SW	347.74	0.60*	0.43	−0.68
TP	271.55	1.18*	0.62	0.25

*Trend at the 5% significant level ($p < 0.05$). SDLR, Surface downward longwave radiation; EC, East China; NC, North China; NE, Northeast China; SC, South China; SW, Southwest China; TP, Tibetan Plateau.

differences occur in NE (147.7 Wm^{-2}), while smaller values occur in SC and SW (66.9 and 68.3 Wm^{-2}, respectively).

4.3.3. Long-Term Trends

Figure 17 demonstrates the trends of the *SDLR* estimates at 563 CMA stations during 1958–2015. The size of each triangle represents the magnitude of the trend, and the red and green triangles indicate increasing and decreasing trends, respectively. Stations with a circle indicate that the trend detected by the MK test is significant at a 95% confidence level. The *SDLR* estimates at stations in central and northern China all showed increasing trends from 1958 to 2015, whereas the *SDLR* estimates at some stations in southern China showed decreasing trends. 549 out of 563 CMA stations show positive trends, and 476 stations increasing significantly during 1958–2015; 14 stations show negative trends, with one stations decreasing significantly. The stations with negative *SDLR* trends were mainly concentrated in SC and SW.

Figure 18 shows the anomalous annual mean *SDLR* estimates averaged over mainland China and the six subregions from 1958 to 2015. A line was fitted to the anomalous annual mean *SDLR* estimates using linear regression. In mainland China, the maximum values occurred in 1998, and the minimum values occurred in 1969. A 1.04 Wm^{-2} per decade increasing linear trend of *SDLR* is observed during the period of 1958–2015. The trends in EC, NC, NE, SW, and TP regions are similar to those over mainland China. In SC, the trend is insignificant but exhibits large interannual variations during the period of 1958–2015.

Since the MK test is more statistically rigorous than the regression method (Mann, 1945), the MK test is used to further analyze the long-term trend. The annual mean *SDLR* estimates over mainland China show significant increasing trends at a rate of 1.02 Wm^{-2} per decade detected by the MK test. The increasing trends are comparable to those from previous studies (Prata, 2008; K. C. Wang & Liang, 2009a). CO_2 is another dominant emitter of *SDLR*, hence the effect of CO_2 on *SDLR* should be considered. The global atmospheric CO_2 concentration has increased by an average of 1.5 ppm per year from 1958 to 2015, which was calculated based on globally averaged marine surface data from the National Oceanic and Atmospheric Administration (NOAA) Earth System Research Laboratory (ESRL) flask network (Laboratory, 2019). The CO_2 concentration increase in China approximately at the same rate as that of global (Administration, 2018). Increasing CO_2 concentration amount by 10% causes ~0.2% (~0.6 Wm^{-2}) increase in *SDLR* (Prata, 2008). If the CO_2 concentration in the atmosphere increases at a rate of 1.5 ppm yr^{-1}, it will result in a corresponding increase in *SDLR* of 0.28 Wm^{-2} per decade. Therefore, the increasing trend of the *SDLR* estimates would be 1.3 Wm^{-2} per decade considering the variability of CO_2 concentration over China. Table 3 also shows that positive values are dominated in most regions. The annual mean *SDLR* estimates in EC, NC, NE, SW and
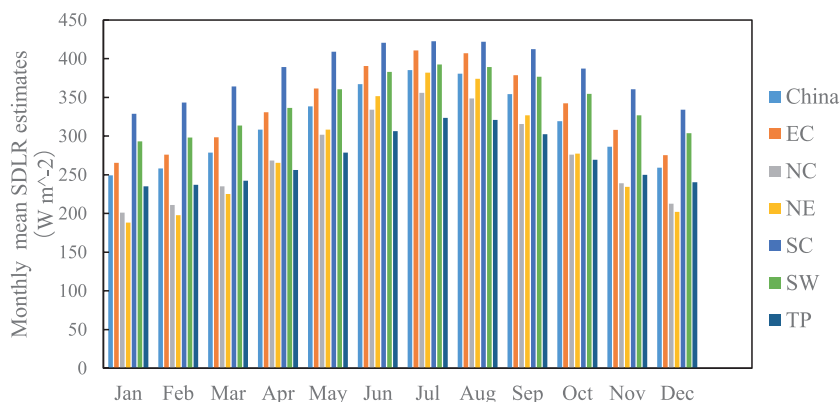
Figure 15. Monthly mean *SDLR* estimates (unit: Wm^{-2}) over the six regions and mainland China during 1958–2015. SDLR, Surface downward longwave radiation.
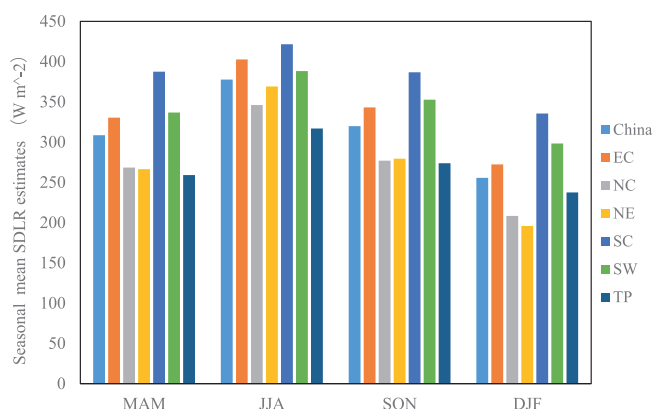
Figure 16. Seasonal mean *SDLR* estimates (unit: Wm^{-2}) over the six regions and mainland China during 1958–2015. SDLR, Surface downward longwave radiation.

TP show significant increasing trends at a rate of 1.07, 1.30, 1.31, 0.60, and 1.18 Wm^{-2} per decade, respectively. SC shows insignificant increasing trends from 1958 to 2015, at a rate of 0.61 Wm^{-2} per decade. It can be seen that most regions over China showed a significant increasing trend from 1958 to 2015, except in SC and SW.

Given the long-term variability in *SDLR*, characterizing various time periods separately may be more useful than linearly fitting the entire time period. Pinker et al. (2005) claimed that the *DSR* showed a decrease until about 1990 and then a sustained increase. Therefore, the annual mean *SDLR* estimates series was divided, with break at 1990. A 0.59 Wm^{-2} per decade insignificant increasing between 1958 and 1990, followed by a 0.59 Wm^{-2} per decade insignificant increasing from 1991 to 2015, was found in anomalous annual mean *SDLR* estimates over mainland China. Annual mean *SDLR* estimates in EC, NC, NE, SC, and TP had very similar trends to mainland China in the specified three time periods, but with different magnitudes. The corresponding values were 0.44 and 0.73 Wm^{-2} for EC, 0.51 and 0.57 Wm^{-2} for NC, 0.41 and 0.94 Wm^{-2} for NE, 0.53 and 0.1 Wm^{-2} for SC, and 0.62 and 0.25 Wm^{-2} for TP. The trends in SW were different from other regions. In SW, there were a 0.43 Wm^{-2} per decade insignificant increasing over 1958–1990, and a 0.68 Wm^{-2} per decade insignificant decreasing over 1991–2015. Before 1990, the anomalous annual mean *SDLR* was negative in most years, but mostly positive after 1990. Therefore, the trends in these two time periods over all subregions are insignificant.

Table 4 summarizes the trends of the seasonal mean *SDLR* estimates over mainland China detected by the MK test from 1958 to 2015. The mean *SDLR* estimates exhibits a positive trend in the four seasons, with the highest rising rate in winter and lowest in summer. The seasonal mean *SDLR* in four season all show insignificant increasing trends from 1958 to 2015, with rates of 0.36, 0.38, 0.45, and 0.99 Wm^{-2} per decade, respectively. We also divided the time period with break at 1990. The seasonal mean *SDLR* estimates in four seasons all showed insignificant increasing over 1958–1990 and significant decreasing over 1991–2015. In spring, there were a 0.13 Wm^{-2} per decade increasing over 1958–1990, and a 3.13 Wm^{-2}
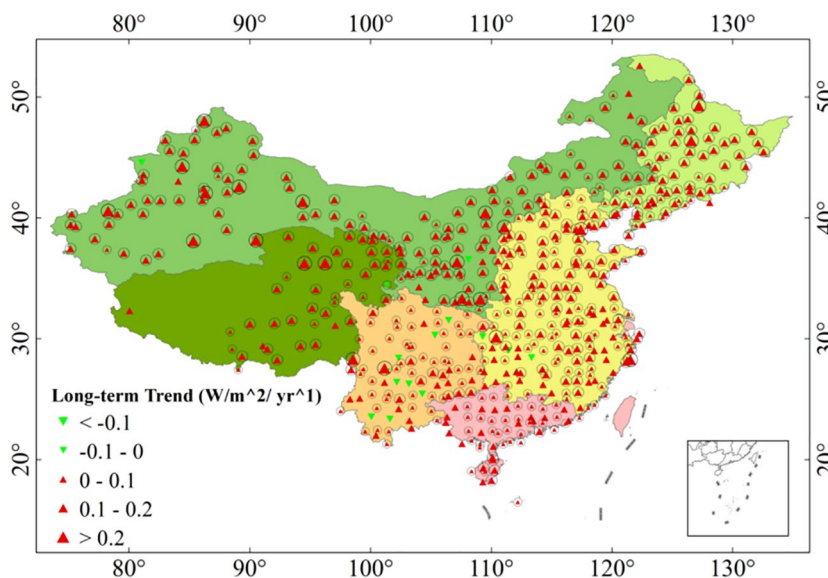
Figure 17. Long-term trends of *SDLR* estimates detected by MK test at 563 CMA stations over 1958–2015. Upward-pointing triangles (red) denote an increasing trend in *SDLR* estimates, whereas downward pointing triangles (green) represent a decreasing trend in *SDLR* estimates. Stations with a circle mean that the trend is significant at the 95% confidence level. CMA, Chinese Meteorological Administration; SDLR, Surface downward longwave radiation.
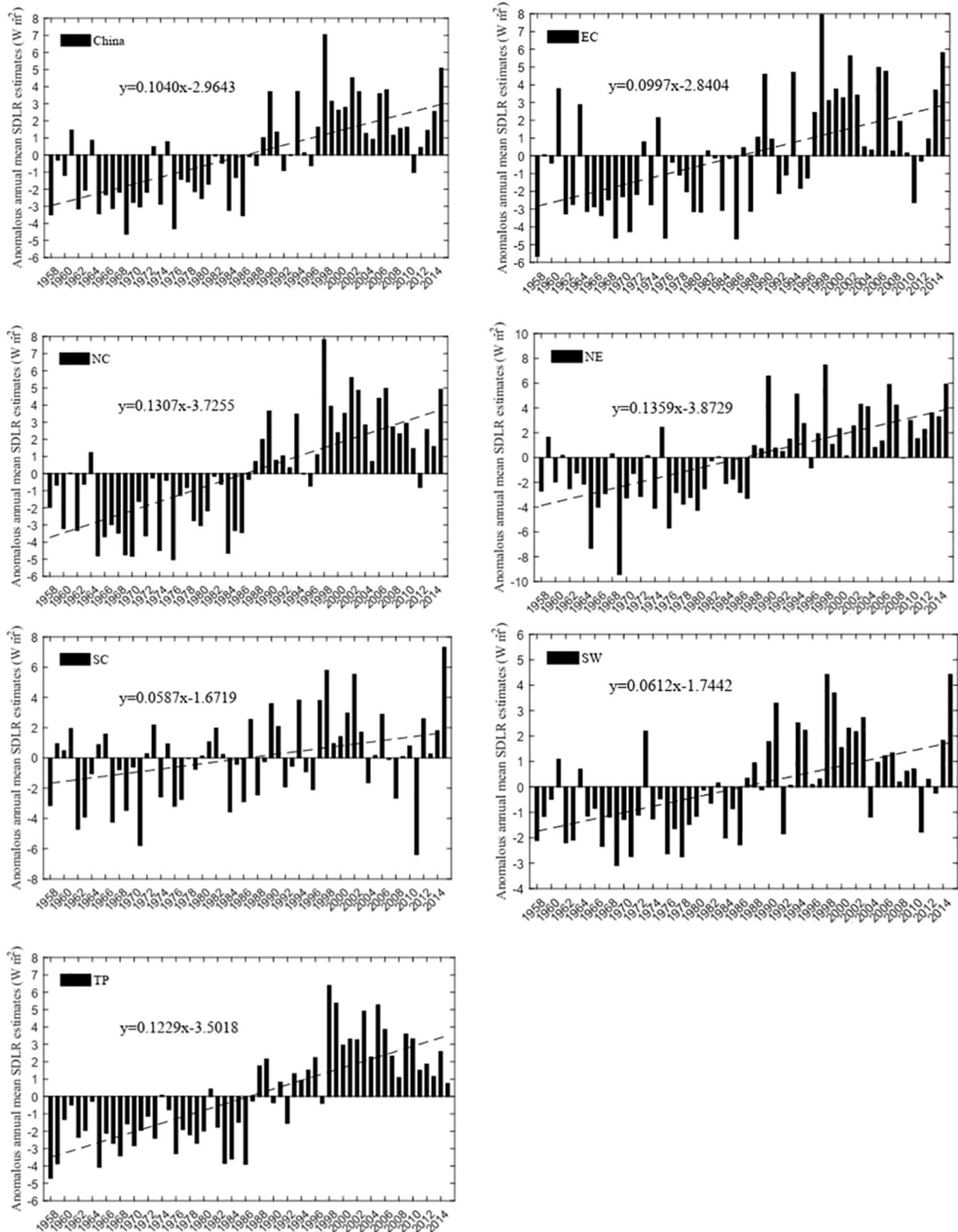
Figure 18. The anomalous annual mean *SDLR* estimates (unit: Wm^{-2}) averaged over each region and mainland China during 1958–2015. SDLR, Surface downward longwave radiation.

Table 4
The Trends in Seasonal Mean SDLR Estimates of Each Season Over Mainland China Detected by MK Test

Season	Seasonal mean SDLR (Wm^{-2})	1958–2015	1958–1990	1991–2015
Spring	309.38	0.36	0.13	−3.13*
Summer	379.20	0.38	0	−3.97*
Autumn	320.52	0.45	0.90	−1.45
Winter	255.60	0.99	1.15	−3.75*

*Trend at the 5% significant level ($p < 0.05$). SDLR, Surface downward longwave radiation.

per decade decreasing over 1991–2015. The corresponding values were 0 and 3.97 Wm^{-2} for summer, 0.9 and 1.45 Wm^{-2} for autumn, 1.15 and 3.75 Wm^{-2} for winter.

5. Discussion

Previous studies suggest that long-term *SDLR* variation is often determined by T_a and atmospheric water vapor concentration (K. C. Wang & Liang, 2009a). In this session, we investigate the correlation between the long-term variation of *SDLR* and other parameters over China. Near surface temperature and water vapor are used to calculate *SDLR* based on the Stefan-Boltzmann equation:

$$SDLR = \left(\varepsilon T_a, e\right)\sigma T_a^4 \tag{8}$$

where σ is the Stefan-Boltzmann constant (5.67×10^{-8} Wm^{-2}K^{-4}). ε is the atmospheric effective emissivity under clear sky conditions. ε can be modeled as a function of T_a, water vapor pressure (e). RH is the ratio of water vapor pressure and saturation water vapor pressure, which can be calculated by T_a using the following equations. We choose water vapor pressure rather than RH to investigate the correlation between the trend in *SDLR*. Under cloudy sky conditions, the cloud cover fraction can also be estimated by the ratio of the measured horizontal global solar radiation to the horizontal global solar radiance under clear sky conditions. Thus, the *DSR* can be used to reflect cloud conditions. Next, the correlation between the trend in *SDLR* and the trend in T_a, water vapor pressure, *DSR* over China from 1958 to 2015 are further explored:

$$RH = \frac{e}{e_s} * 100\%, \tag{9}$$

$$e_s = 6.11 \exp\left(\frac{L_v}{R_v}\left(\frac{1}{273} - \frac{1}{Ta}\right)\right), \tag{10}$$

where e and e_s are the water vapor pressure and the saturation water vapor pressure, respectively.

Figure 19 shows the time series of anomalous annual mean *SDLR* estimates, measured T_a, calculated water vapor pressure and measured *DSR* from 1958 to 2015 over China. It is shown that the trend of *SDLR* is generally consistent with the trend of T_a and water vapor pressure, whereas the trend of *SDLR* is opposite to the trend of *DSR*. To fully assess the causes of changes in *SDLR*, we further quantitatively investigated the correlation between the *SDLR* and other variables. Figure 20 is the scatterplots of the trend in *SDLR* estimates detected by the MK test as a function of the trends in T_a, water vapor pressure, and *DSR* at the 563 CMA stations. One point in the figure represents one station. The trend of *SDLR* is positively correlated with the trends in T_a and water vapor pressure, and the R values between *SDLR* with T_a and vapor pressure are 0.62 and 0.60, respectively. The trend of *SDLR* is negatively correlated with the trend in *DSR*, with an R value of −0.16. *SDLR* is not strongly correlated with *DSR* over mainland China during the period of 1958–2015.

In order to study the characteristics of parameters which controlling the long-term variation of *SDLR* in different regions over China, the correlation of the trends in *SDLR* with the trends in T_a, water vapor pressure and *DSR* over the six regions is also shown in Figure 21. The trend of *SDLR* is positively correlated with the trend in T_a and water vapor pressure, whereas it is negatively correlated with the trend in *DSR* in all sub-regions. In EC and TP, the trend of *SDLR* is highly correlated with the trend of T_a, with R values of 0.65. In EC, NE, SC, SW, and TP, the trend of *SDLR* is highly correlated with the trend of water vapor pressure, with an R value of 0.63, 0.72, 0.70, 0.75, and 0.69, respectively. In TP, the trend of *SDLR* exhibits a relatively high negative correlation with the trend of *DSR*, with R values of −0.57. The trend of *SDLR* has no significant correlation with the trend of T_a, water vapor pressure and *DSR* in NC. These results suggest that the primary controlling factors of the *SDLR* long-term variation for six climatic zones were different: the increases in water vapor pressure results to the rising trend over most subregions, the rising trend over TP mainly results from both increases in T_a and water vapor pressure and decreases in *DSR*, the rising trend over NC has no
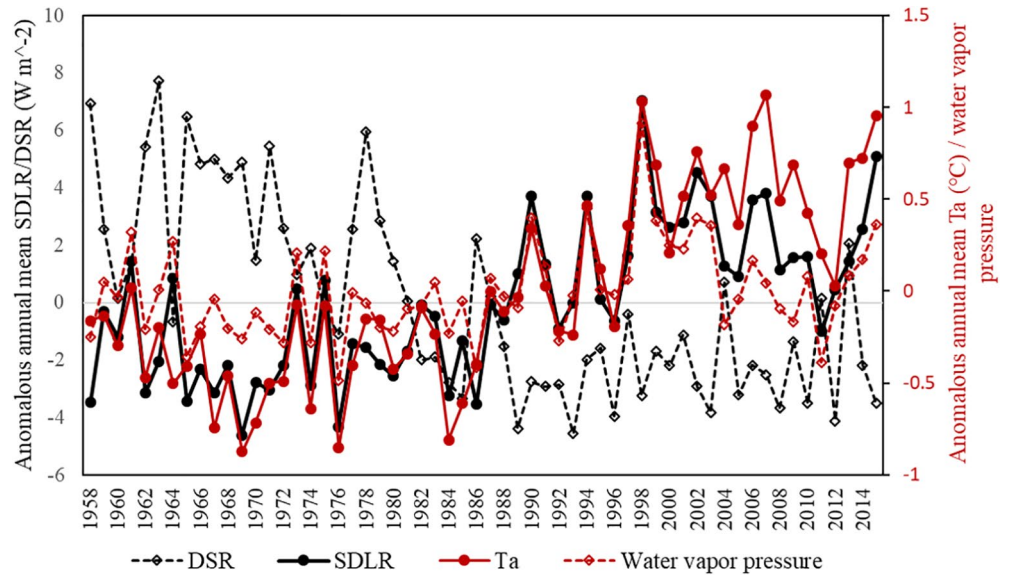
Figure 19. Anomalous annual mean *SDLR* estimates, measured T_a, calculated water vapor pressure and measured *DSR* during 1958–2015 over China. DSR, downward shortwave radiation; SDLR, Surface downward longwave radiation.

significant correlation with those of other three variables. It is noted that the number of samples over each region is quite limited based on the completeness of the data records, and the points are scattered and uneven, which may lead to errors in the results.

6. Conclusions

SDLR is a major component of the energy budget in the Earth's climate system. However, *SDLR* is not conventionally observed due to the high cost and difficulty of a direct measurement. It has great significance to generate a comprehensively spatiotemporal extended *SDLR* data set over China based on more readily available data has. In this study, we reconstructed *SDLR* based on the GBRT method using T_a, RH and *DSR*. Daily ground measurements collected at the BSRN and ASRCOP stations were used to build and validate the GBRT model, respectively. The evaluation results showed that the estimated *SDLRs* using the GBRT method correlate well with the *SDLR* in situ, with an overall RMSE of 16.5 Wm^{-2} and an *R* value of 0.91 at a daily time scale. Thus, applying the GBRT method to estimate *SDLR* provides reasonable and realistic radiation quantity and its variation without a local correlation.
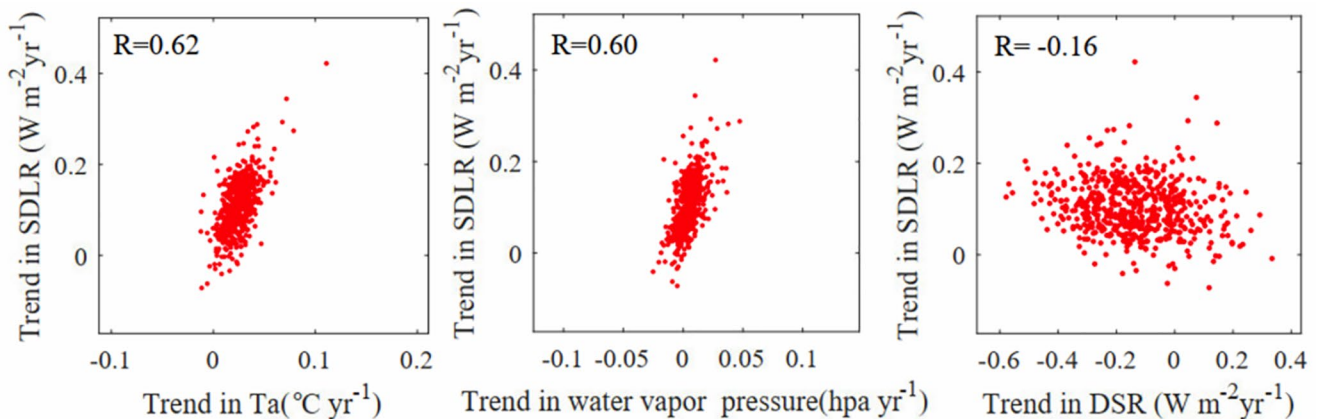
Figure 20. The scatterplots of trends in *SDLR* (unit: W/m²/yr) as a function of trends in (a) T_a, (b) water vapor pressure, and (c) *DSR* at the stations. DSR, downward shortwave radiation; SDLR, Surface downward longwave radiation.
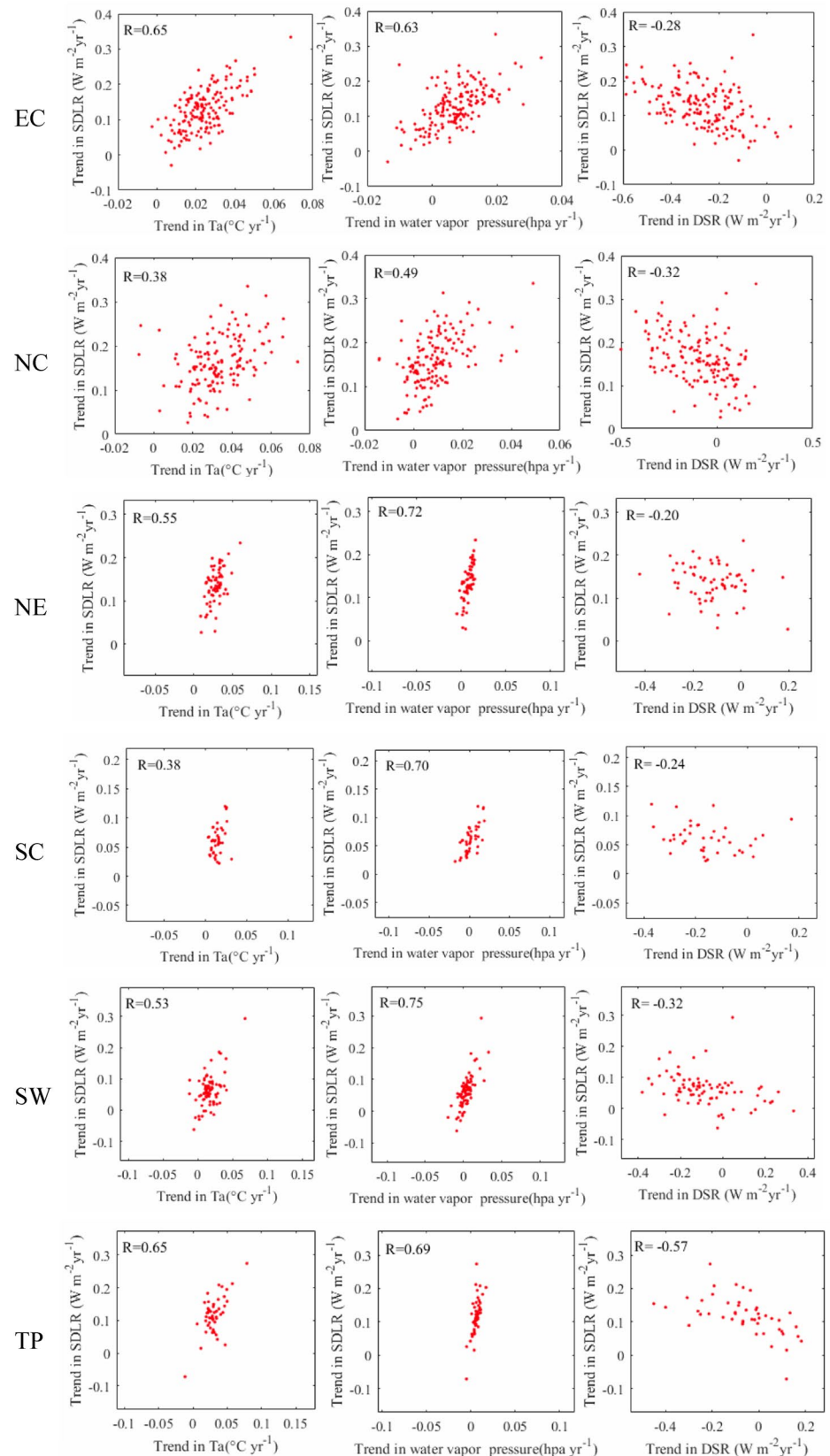
Figure 21. The scatterplots of trends in *SDLR* as a function of trends in T_a, water vapor pressure and *DSR* over six regions. DSR, downward shortwave radiation; SDLR, Surface downward longwave radiation.

To obtain long-term *SDLR* data for subsequent spatiotemporal analysis based on the proposed method over China, the densely distributed reconstructed *DSR* and ground measured T_a and RH collected at 756 CMA stations were used as input to estimate the *SDLR* based on the GBRT method over China from 1958 to 2015. We also analyzed the spatial pattern and temporal variations of the estimated *SDLRs* at 563 CMA stations over China where the data were relatively complete during the period of 1958–2015. The maximum annual mean *SDLR* occurred in SC, whereas the minimum value occurred in TP. The seasonal mean *SDLR* estimates were highest in summer and lowest in winter. The spatial distribution of the estimated *SDLRs* in each season was similar to that in the whole year. It was found that *SDLR* increased significantly at an average rate of 1.3 Wm^{-2} per decade from 1958 to 2015 as detected by the MK test. The long-term trends in most regions were consistent with those in the whole China area, except for SC. In SC, the annual mean *SDLR* exhibited insignificant increasing trends at a rate of 0.61 Wm^{-2} per decade. We also compared the accuracy and trends of the *SDLR* estimates based on the GBRT method between those from existing *SDLR* products. The comparison result showed that accuracy and trends of the estimated *SDLRs* of the GBRT method are reasonable.

The primary controlling factors of the *SDLR* long-term variation was investigated in mainland China by analyzing the correlation between the trend of *SDLR* and the trends of T_a, water vapor pressure, and *DSR* at the 563 CMA stations. The trend of *SDLR* was generally positively correlated with the trend in T_a and water vapor pressure, negatively correlated with the trend in *DSR*. The primary controlling factors of the *SDLR* long-term variation for six climatic zones were different.

Although the GBRT method is robust to outliers in output space, and has been efficient and practical for many research applications, the GBRT method also has some disadvantages. First, the GBRT method has poor scalability due to the order nature of its promotion. Second, the training procedure is sensitive to the choice of parameters. There is a trade-off between overfitting and computational cost. The step size of learning rate parameter may need to be small to avoid overfitting. However, the small learning rate parameter may imply a high computational cost of applications. Thus other machine learning methods or deep learning methods can be further explored to improve accuracy and efficiency of *SDLR* estimation.

The density of the *SDLR* measurements is sparser than that of the meteorological and *DSR* measurements. The *SDLR* can be estimated and easily extended to more stations and over longer time periods using the GBRT method without a local correlation. This study only applies the GBRT method at stations using ground measurements. However, the number and spatial distribution of the training samples may have influence on *SDLR* estimation. We plan to extend the GBRT method for *SDLR* estimation from stations to surface, using reanalysis data and/or retrievals from satellite observations.

Data Availability Statement

The ground measurements at CMA stations are available at http://cdc.nmic.cn/home.do; the ground measurements at BSRN stations are available at https://dataportals.pangaea.de/bsrn; the CERES-SYN data are available at https://ceres.larc.nasa.gov/; the ERA5 data are available at https://www.ecmwf.int/en/forecasts/datasets/reanalysis-datasets/era5; the GEWEX-SYN data are available at http://www.gewex.org/data-sets-surface-radiation-budget-srb/.

References

Ackerman, S. A., Holz, R. E., Frey, R., Eloranta, E. W., Maddux, B. C., & McGill, M. (2008). Cloud detection with MODIS. Part II: Validation. *Journal of Atmospheric and Oceanic Technology*, *25*(7), 1073–1086. https://doi.org/10.1175/2007jtecha1053.1

Aladosarboledas, L. (1993). Estimation of hourly values of downward atmospheric radiation under cloudless skies during daytime and nighttime conditions. *Theoretical and Applied Climatology*, *48*(2-3), 127–131. https://doi.org/10.1007/bf00864919

Bilbao, J., & De Miguel, A. H. (2007). Estimation of daylight downward longwave atmospheric irradiance under clear-sky and all-sky conditions. *Journal of Applied Meteorology and Climatology*, *46*(6), 878–889. https://doi.org/10.1175/jam2503.1

Brunt, D. (1932). Notes on radiation in the atmosphere. *Quarterly Journal of the Royal Meteorological Society*, *58*(247), 389–420. https://doi.org/10.1002/qj.49705824704

Brutsaert, W. (1975). Derivable formula for long-wave radiation from clear skies. *Water Resources Research*, *11*(5), 742–744. https://doi.org/10.1029/wr011i005p00742

Burt, M. A., Randall, D. A., & Branson, M. D. (2016). Dark warming. *Journal of Climate*, *29*(2), 705–719. https://doi.org/10.1175/jcli-d-15-0147.1

Chang, K., & Zhang, Q. Y. (2019). Modeling of downward longwave radiation and radiative cooling potential in China. *Journal of Renewable and Sustainable Energy*, *11*(6), 11. https://doi.org/10.1063/1.5117319

Cheng, J., & Liang, S. L. (2016). Global estimates for high-spatial-resolution clear-sky land surface upwelling longwave radiation from MODIS data. *IEEE Transactions on Geoscience and Remote Sensing*, *54*(7), 4115–4129. https://doi.org/10.1109/tgrs.2016.2537650

Cheng, J., Liang, S. L., Wang, W. H., & Guo, Y. M. (2017). An efficient hybrid method for estimating clear-sky surface downward longwave radiation from MODIS data. *Journal of Geophysical Research: Atmospheres*, *122*(5), 2616–2630. https://doi.org/10.1002/2016jd026250

China Meteorological Administration: Climate Change Centre. (2018). *2016 China Greenhouse Gas Bulletin*.

Cox, S. J., Stackhouse, P., Gupta, S., Mikovitz, J., Zhang, T., Hinkelman, L., et al. (2006). *The NASA/GEWEX surface radiation budget project: Overview and analysis*. Madison, WI: The 12th Conference on Atmospheric Radiation.

Crawford, T. M., & Duchon, C. E. (1999). An improved parameterization for estimating effective atmospheric emissivity for use in calculating daytime downwelling longwave radiation. *Journal of Applied Meteorology*, *38*(4), 474–480. https://doi.org/10.1175/1520-0450(1999)038<0474:aipfee>2.0.co;2

Darnell, W. L., Gupta, S. K., & Staylor, W. F. (1983). Downward longwave radiation at the surface from satellite measurements. *Journal of Climate and Applied Meteorology*, *22*(11), 1956–1960. https://doi.org/10.1175/1520-0450(1983)022<1956:dlrats>2.0.co;2

Diak, G. R., Bland, W. L., Mecikalski, J. R., & Anderson, M. C. (2000). Satellite-based estimates of longwave radiation for agricultural applications. *Agricultural and Forest Meteorology*, *103*(4), 349–355. https://doi.org/10.1016/s0168-1923(00)00141-6

Dilley, A. C., & O'Brien, D. M. (1998). Estimating downward clear sky longlite-based estimates of longwave radiation for agricultural applicable water. *Quarterly Journal of the Royal Meteorological Society*, *124*(549), 1391–1401. https://doi.org/10.1002/qj.49712454903

Ding, C., Wang, D. G., Ma, X. L., & Li, H. Y. (2016). Predicting short-term subway ridership and prioritizing its influential factors using gradient boosting decision trees. *Sustainability*, *8*(111), 1100. https://doi.org/10.3390/su8111100

Doelling, D. R., Loeb, N. G., Keyes, D. F., Nordeen, M. L., Morstad, D., Nguyen, C., et al. (2013). Geostationary enhanced temporal interpolation for CERES flux products. *Journal of Atmospheric and Oceanic Technology*, *30*(6), 1072–1090. https://doi.org/10.1175/jtech-d-12-00136.1

Duarte, H. F., Dias, N. L., & Maggiotto, S. R. (2006). Assessing daytime downward longwave radiation estimates for clear and cloudy skies in Southern Brazil. *Agricultural and Forest Meteorology*, *139*(3-4), 171–181. https://doi.org/10.1016/j.agrformet.2006.06.008

Ellingson, R. G. (1995). Surface longwave fluxes from satellite-observations: A critical-review. *Remote Sensing of Environment*, *51*(1), 89–97. https://doi.org/10.1016/0034-4257(94)00067-w

Enz, J. W., Klink, J. C., & Baker, D. G. (1975). Solar-radiation effects on pyrgeometer performance. *Journal of Applied Meteorology*, *14*(7), 1297–1302. https://doi.org/10.1175/1520-0450(1975)014<1297:sreopp>2.0.co;2

Flerchinger, G. N., Xaio, W., Marks, D., Sauer, T. J., & Yu, Q. (2009). Comparison of algorithms for incoming atmospheric long-wave radiation. *Water Resources Research*, *45*(3), 13. https://doi.org/10.1029/2008wr007394

Gocic, M., & Trajkovic, S. (2013). Analysis of changes in meteorological variables using Mann-Kendall and Sen's slope estimator statistical tests in Serbia. *Global and Planetary Change*, *100*, 172–182. https://doi.org/10.1016/j.gloplacha.2012.10.014

Guo, Y. M., Cheng, J., & Liang, S. L. (2019). Comprehensive assessment of parameterization methods for estimating clear-sky surface downward longwave radiation. *Theoretical and Applied Climatology*, *135*(3-4), 1045–1058. https://doi.org/10.1007/s00704-018-2423-7

Gupta, S. K., Kratz, D. P., Wilber, A. C., & Nguyen, L. C. (2004). Validation of parameterized algorithms used to derive TRMM-CERES surface radiative fluxes. *Journal of Atmospheric and Oceanic Technology*, *21*(5), 742–752. https://doi.org/10.1175/1520-0426(2004)021<0742:vopaut>2.0.co;2

Hersbach, H., & Dee, D. (2016). ERA5 reanalysis is in production. *ECMWF Newsletter*, *147*, 7.

He, J., Yang, K., Tang, W. J., Lu, H., Qin, J., Chen, Y. Y., & Li, X. (2020). The first high-resolution meteorological forcing dataset for land process studies over China. *Scientific Data*, *7*(1), 11. https://doi.org/10.1038/s41597-020-0369-y

Hou, N., Zhang, X., Zhang, W., Xu, J., Feng, C., Yang, S., et al. (2020). A New Long-Term Downward Surface Solar Radiation Dataset over China from 1958 to 2015. *Sensors*, *20*, 6167.

Huang, G. H., Wang, W. Z., Zhang, X. T., Liang, S. L., Liu, S. M., Zhao, T. B., et al. (2013). Preliminary validation of GLASS-DSSR products using surface measurements collected in arid and semi-arid regions of China. *International Journal of Digital Earth*, *6*, 50–68. https://doi.org/10.1080/17538947.2013.825655

Idso, S. B. (1981). A set of equations for full spectrum and 8- to 14-μm and 10.5- to 12.5-μm thermal-radiation from cloudless skies. *Water Resources Research*, *17*(2), 295–304. https://doi.org/10.1029/wr017i002p00295

Iziomon, M. G., Mayer, H., & Matzarakis, A. (2003). Downward atmospheric longwave irradiance under clear and cloudy skies: Measurement and parameterization. *Journal of Atmospheric and Solar-Terrestrial Physics*, *65*(10), 1107–1116. https://doi.org/10.1016/j.jastp.2003.07.007

Johnson, R., & Zhang, T. (2014). Learning nonlinear functions using regularized greedy forest. *IEEE Transactions on Pattern Analysis and Machine Intelligence*, *36*(5), 942–954. https://doi.org/10.1109/tpami.2013.159

Kendall, M. G. (1938). A new measure of rank correlation. *Biometrika*, *30*, 81–93. https://doi.org/10.2307/2332226

Laboratory, N. E. S. R.. (2019). The NOAA annual greenhouse gas index (AGGI).

Liang, S. L., Wang, K. C., Zhang, X. T., & Wild, M. (2010). Review on estimation of land surface radiation and energy budgets from ground measurement, remote sensing and model simulations. *IEEE Journal of Selected Topics in Applied Earth Observations and Remote Sensing*, *3*(3), 225–240. https://doi.org/10.1109/jstars.2010.2048556

Liu, Z. J., Liu, Y. S., Wang, S. S., Yang, X. J., Wang, L. C., Baig, M. H. A., et al. (2018). Evaluation of spatial and temporal performances of ERA-interim precipitation and temperature in Mainland China. *Journal of Climate*, *31*(11), 4347–4365. https://doi.org/10.1175/jcli-d-17-0212.1

Mann, H. B. (1945). Nonparametric tests against trend. *Econometrica*, *13*(3), 245–259. https://doi.org/10.2307/1907187

Maykut, G. A., & Church, P. E. (1973). Radiation Climate of Barrow Alaska, 1962-66. *Journal of Applied Meteorology*, *12*(4), 620–628. https://doi.org/10.1175/1520-0450(1973)012<0620:rcoba>2.0.co;2

Moradi, I. (2009). Quality control of global solar radiation using sunshine duration hours. *Energy*, *34*(1), 1–6. https://doi.org/10.1016/j.energy.2008.09.006

Naseef, T. M., & Kumar, V. S. (2008). Climatology and trends of the Indian Ocean surface waves based on 39-year long ERA5 reanalysis data. *International Journal of Climatology*, *40*(2), 979–1006. https://doi.org/10.1002/joc.6251

Niemela, S., Raisanen, P., & Savijarvi, H. (2001). Comparison of surface radiative flux parameterizations - Part I: Longwave radiation. *Atmospheric Research*, *58*(1), 1–18. https://doi.org/10.1016/s0169-8095(01)00084-9

Ohmura, A., Dutton, E. G., Forgan, B., Frohlich, C., Gilgen, H., Hegner, H., et al. (1998). Baseline surface radiation network (BSRN/WCRP): New precision radiometry for climate research. *Bulletin of the American Meteorological Society*, *79*(10), 2115–2136. https://doi.org/10.1175/1520-0477(1998)079<2115:bsrnbw>2.0.co;2

Pedregosa, F., Gramfort, A., Michel, V., Thirion, B., Grisel, O., Blondel, M., et al. (2012). Scikit-learn: Machine Learning in Python. *Journal of Machine Learning Research*, *12*, 2825–2830.

Pendergrass, A. G., Conley, A., & Vitt, F. M. (2018). Surface and top-of-atmosphere radiative feedback kernels for CESM-CAM5. *Earth System Science Data*, *10*(1), 317–324. https://doi.org/10.5194/essd-10-317-2018

Pinker, R. T., Zhang, B., & Dutton, E. G. (2005). Do satellites detect trends in surface solar radiation?. *Science*, *308*(5723), 850–854. https://doi.org/10.1126/science.1103159

Prata, F. (2008). The climatological record of clear-sky longwave radiation at the Earth's surface: Evidence for water vapour feedback?. *International Journal of Remote Sensing*, *29*(17-18), 5247–5263. https://doi.org/10.1080/01431160802036508

Previdi, M. (2010). Radiative feedbacks on global precipitation. *Environmental Research Letters*, *5*(2), 11. https://doi.org/10.1088/1748-9326/5/2/025211

Sen, P. K. (1968). Estimates of regression coefficient based on Kendall's tau. *Journal of the American Statistical Association*, *63*(324), 1379–1389. https://doi.org/10.1080/01621459.1968.10480934

Sridhar, V., & Elliott, R. L. (2002). On the development of a simple downwelling longwave radiation scheme. *Agricultural and Forest Meteorology*, *112*(3-4), 237–243. https://doi.org/10.1016/s0168-1923(02)00129-6

Stephens, G. L., Slingo, A., Webb, M. J., Minnett, P. J., Daum, P. H., Kleinman, L., et al. (1994). Observations of the earths radiation budget in relation to atmospheric hydrology .4. Atmospheric column radiative cooling over the world's oceans. *Journal of Geophysical Research*, *99*(D9), 18585–18604. https://doi.org/10.1029/94jd01151

Swinbank, W. C. (1963). Long-wave radiation from clear skies. *Quarterly Journal of the Royal Meteorological Society*, *89*(381), 339–348. https://doi.org/10.1002/qj.49708938105

Tang, B., & Li, Z. L. (2008). Estimation of instantaneous net surface longwave radiation from MODIS cloud-free data. *Remote Sensing of Environment*, *112*(9), 3482–3492. https://doi.org/10.1016/j.rse.2008.04.004

Tang, W. J., Yang, K., He, J., & Qin, J. (2010). Quality control and estimation of global solar radiation in China. *Solar Energy*, *84*(3), 466–475. https://doi.org/10.1016/j.solener.2010.01.006

Tang, W. J., Yang, K., Qin, J., & Min, M. (2013). Development of a 50-year daily surface solar radiation dataset over China. *Science China Earth Sciences*, *56*(9), 1555–1565. https://doi.org/10.1007/s11430-012-4542-9

Wang, K., & Dickinson, R. E. (2013). Global atmospheric downward longwave radiation at the surface from ground-based observations, satellite retrievals, and reanalyses. *Reviews of Geophysics*, *51*(2), 150–185. https://doi.org/10.1002/rog.20009

Wang, K. C., & Liang, S. L. (2009a). Global atmospheric downward longwave radiation over land surface under all-sky conditions from 1973 to 2008. *Journal of Geophysical Research*, *114*(D19), 12. https://doi.org/10.1029/2009jd011800

Wang, W. H., & Liang, S. L. (2009b). Estimation of high-spatial resolution clear-sky longwave downward and net radiation over land surfaces from MODIS data. *Remote Sensing of Environment*, *113*(4), 745–754. https://doi.org/10.1016/j.rse.2008.12.004

Wang, T. X., Shi, J. C., Yu, Y. C., Husi, L., Gao, B., Zhou, W., et al. (2018). Cloudy-sky land surface longwave downward radiation (LWDR) estimation by integrating MODIS and AIRS/AMSU measurements. *Remote Sensing of Environment*, *205*, 100–111. https://doi.org/10.1016/j.rse.2017.11.011

Wang, J., Tang, B. H., Zhang, X. Y., Wu, H., & Li, Z. L. (2014). Estimation of surface longwave radiation over the Tibetan Plateau region using MODIS data for cloud-free skies. *IEEE Journal of Selected Topics in Applied Earth Observations and Remote Sensing*, *7*(9), 3695–3703. https://doi.org/10.1109/jstars.2014.2320585

Wang, T. X., Yan, G. J., & Chen, L. (2012). Consistent retrieval methods to estimate land surface shortwave and longwave radiative flux components under clear-sky conditions. *Remote Sensing of Environment*, *124*, 61–71. https://doi.org/10.1016/j.rse.2012.04.026

Wang, X. Y., Yao, Y. J., Zhao, S. H., Jia, K., Zhang, X. T., Zhang, Y. H., et al. (2017). MODIS-based estimation of terrestrial latent heat flux over North America using three machine learning algorithms. *Remote Sensing*, *9*(12), 1326. https://doi.org/10.3390/rs9121326

Wei, Y., Zhang, X. T., Hou, N., Zhang, W. Y., Jia, K., & Yao, Y. J. (2019). Estimation of surface downward shortwave radiation over China from AVHRR data based on four machine learning methods. *Solar Energy*, *177*, 32–46. https://doi.org/10.1016/j.solener.2018.11.008

Woods, C., & Caballero, R. (2016). The role of moist intrusions in winter arctic warming and sea ice decline. *Journal of Climate*, *29*(12), 4473–4485. https://doi.org/10.1175/jcli-d-15-0773.1

Yang, K., He, J., Tang, W. J., Qin, J., & Cheng, C. C. K. (2010). On downward shortwave and longwave radiations over high altitude regions: Observation and modeling in the Tibetan Plateau. *Agricultural and Forest Meteorology*, *150*(1), 38–46. https://doi.org/10.1016/j.agrformet.2009.08.004

Yang, L., Zhang, X. T., Liang, S. L., Yao, Y. J., Jia, K., & Jia, A. L. (2018). Estimating surface downward shortwave radiation over china based on the gradient boosting decision tree method. *Remote Sensing*, *10*(2), 185. https://doi.org/10.3390/rs10020185

Yu, S. S., Xin, X. Z., Liu, Q. H., Zhang, H. L., & Li, L. (2018). Comparison of cloudy-sky downward longwave radiation algorithms using synthetic data, ground-based data, and satellite data. *Journal of Geophysical Research: Atmospheres*, *123*(10), 5397–5415. https://doi.org/10.1029/2017jd028234

Zeppetello, L. R. V., Donohoe, A., & Battisti, D. S. (2019). Does surface temperature respond to or determine downwelling longwave radiation?. *Geophysical Research Letters*, *46*(5), 2781–2789. https://doi.org/10.1029/2019gl082220

Zhang, X. T., Liang, S. L., Wild, M., & Jiang, B. (2015). Analysis of surface incident shortwave radiation from four satellite products. *Remote Sensing of Environment*, *165*, 186–202. https://doi.org/10.1016/j.rse.2015.05.015

Zhou, Z. G., Wang, L. C., Lin, A. W., Zhang, M., & Niu, Z. G. (2018). Innovative trend analysis of solar radiation in China during 1962-2015. *Renewable Energy*, *119*, 675–689. https://doi.org/10.1016/j.renene.2017.12.052